Science
AAAS

Supplementary Materials for

Nucleolar maturation of the human small subunit processome

Sameer Singh *et al.*

Corresponding authors: Arnaud Vanden Broeck, avanden@rockefeller.edu; Sebastian Klinge, klinge@rockefeller.edu

Science **373**, eabj5338 (2021)
DOI: 10.1126/science.abj5338

The PDF file includes:

Other Supplementary Material for this manuscript includes the following:

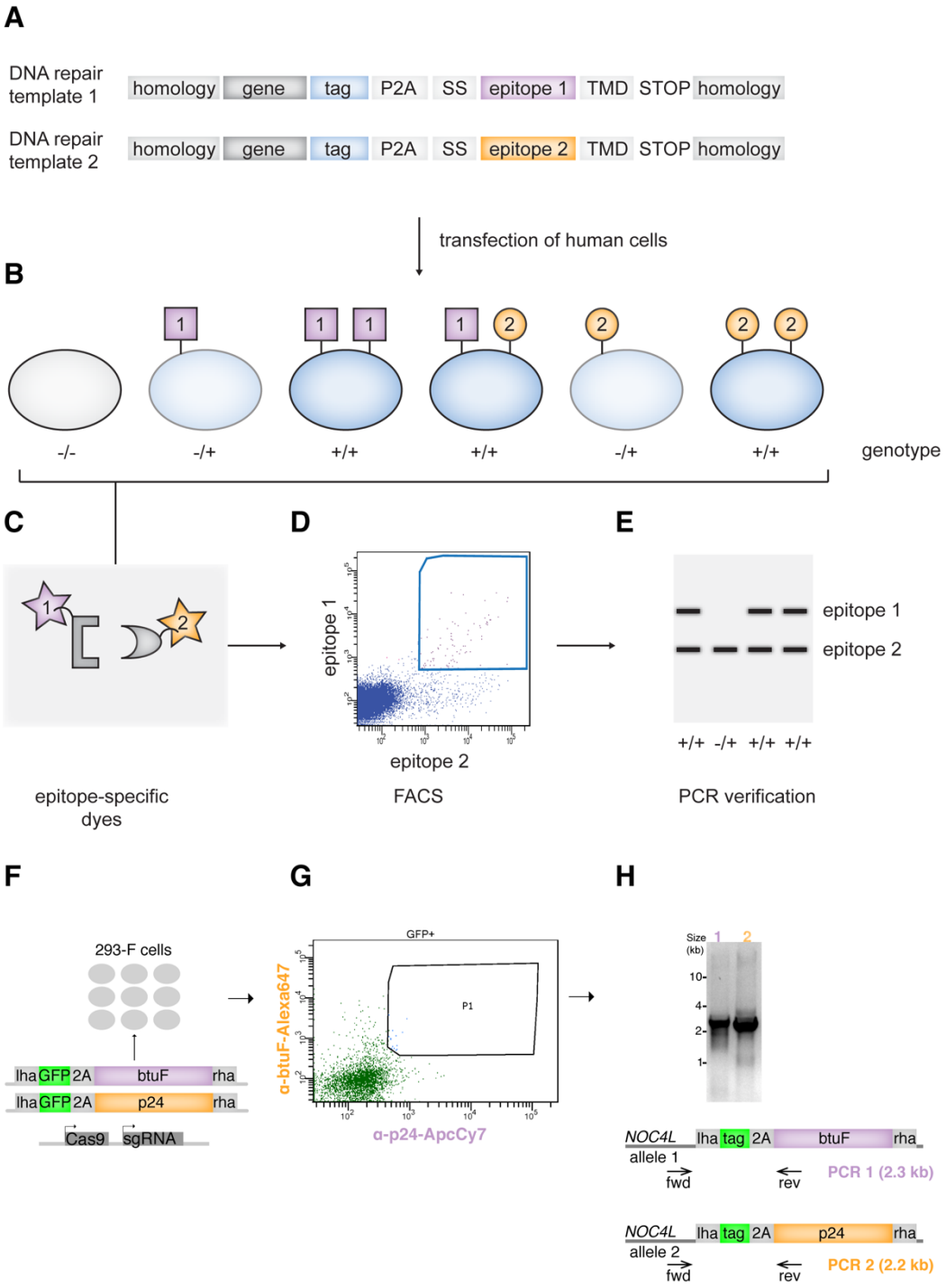

Fig. S1. Human genome editing with SNEAK PEEC.

(**A**) Architecture of the repair templates used for biallelic tagging using SNEAK PEEC. Each repair template contains a left homology arm, a portion of the last exon of the gene (gene), a C-terminal tag (tag), a self-cleaving peptide sequence (P2A), a cell-surface display epitope (SS-epitope1/2-TMD) and a right homology arm (**B**). Transfection of human cells with the two DNA repair templates and Cas9+sgRNA can result in six different outcomes of cells either containing no edited gene or different monoallelic (-/+)

or biallelic (+/+) combinations. Cells harboring both surface displays represent a biallelically edited clone. (**C**, **D**) Cells are surface stained using epitope-specific dyes and sorted for single cell clones expressing both surface displays. (**E**) Isolated single clones are genotyped to confirm the genomic integration of both repair templates. (**F**) Transfection of 293-F cells with plasmids containing two repair templates targeting the C-terminus of the NOC4L gene, along with a plasmid expressing Cas9+sgRNA. Each repair template encodes GFP followed by a unique surface display epitope (btuF or p24). (**G**) FACS sorting of transfected cells pre-stained with fluorescent nanobodies (α-btuF-Alexa647, α-p24-ApcCy7**)**. Single cell clones were selected for expression of GFP and the two surface display epitopes. (**H**) A biallelically edited clone was identified using two PCR reactions that confirm the integration of a different repair template at each NOC4L allele.

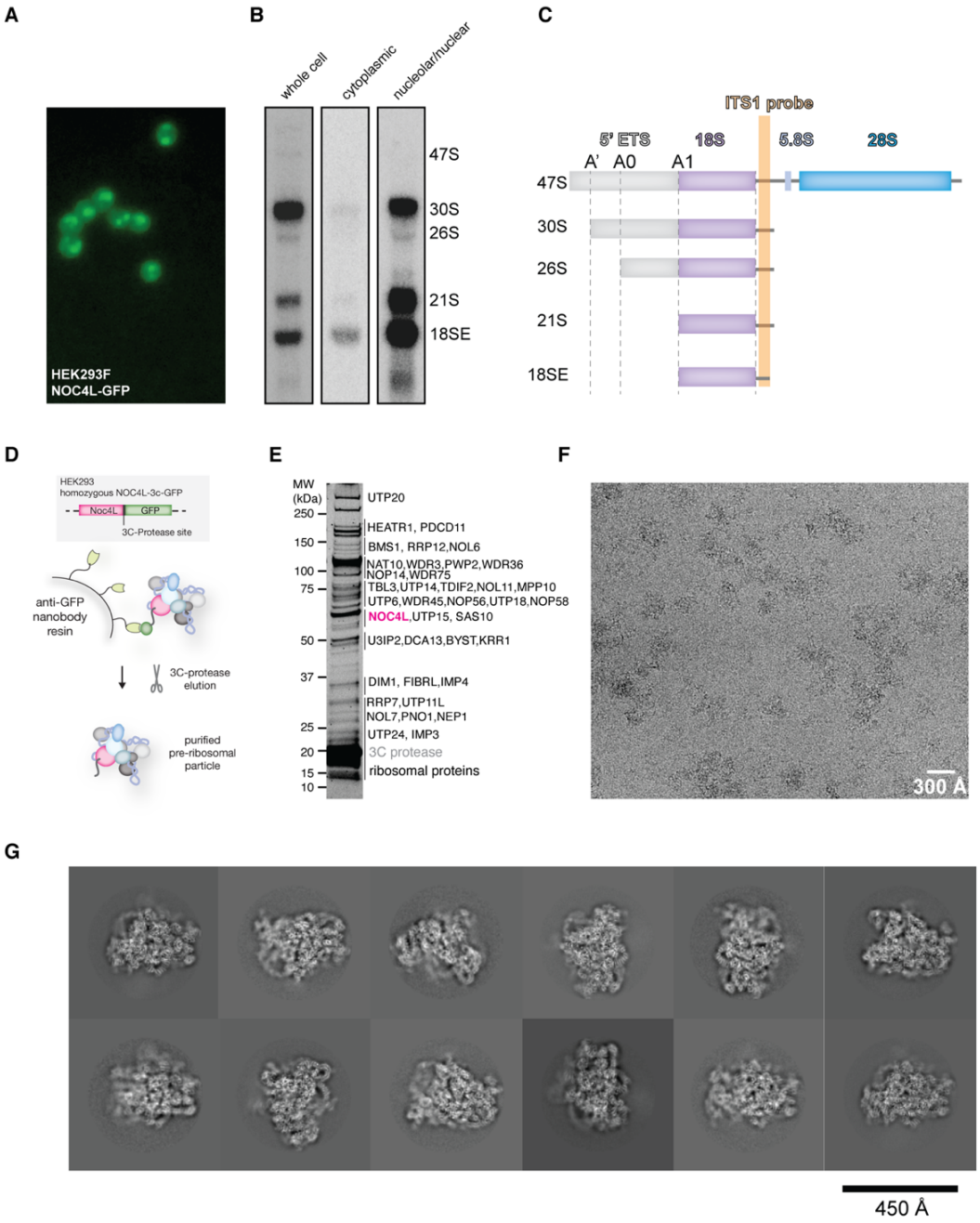

Fig. S2. Purification of human SSU processomes.

(**A**) Fluorescence microscopy image of the NOC4L-GFP 293-F cell line. (**B**) Northern blot analysis of pre-rRNAs species present in the whole cell fraction as well as those extracted by sequential lysis. A probe hybridizing within ITS1 was used. (**C**) Schematic of pre-rRNAs species detected using the ITS1 probe. The positions of RNA cleavage sites are indicated above. (**D**) Schematic of a one-step purification strategy to isolate human NOC4L-GFP tagged pre-ribosomal particles. (**E**) SYPRO Ruby stained SDS-PAGE analysis of purified fraction containing pre-ribosomal particles. Bait protein (NOC4L; pink) and molecular weight markers are indicated on the left (MW). (**F**) A representative cryo-EM micrograph. (**G**) Unsupervised 2D class averages.

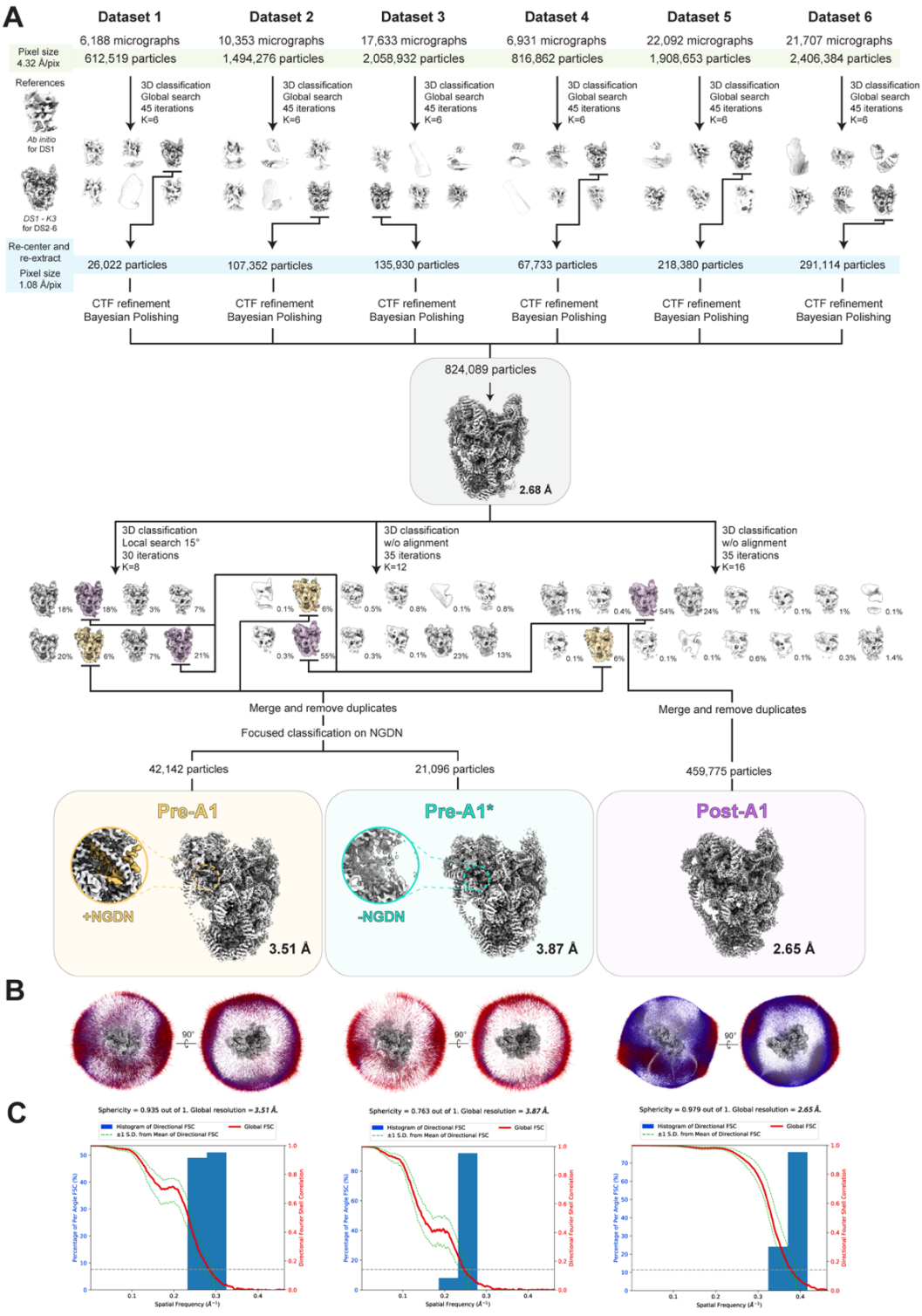

Fig. S3. Structure determination of human SSU processomes.

(A) Cryo-EM data processing workflow for the structure determination of human SSU processomes. **(B)** Euler angle distribution of human SSU processomes reconstructions. Each cone represents a view, the height being proportional to the number of particles contributing to that view. **(C)** 3D-FSC curve (*74*) for each reconstruction.

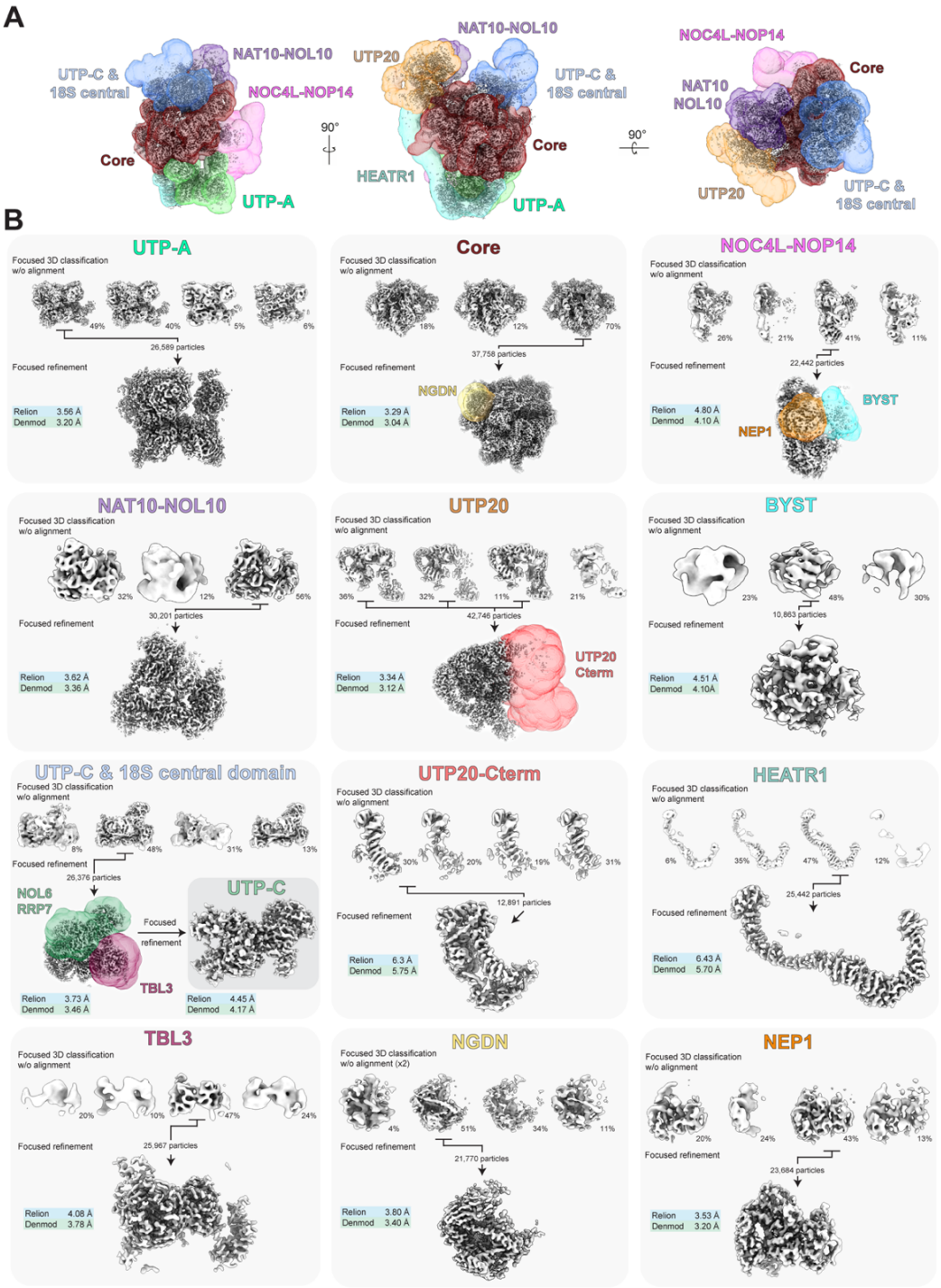

Fig. S4. Cryo-EM processing of state pre-A1.

(**A**) Cryo-EM structure of the human SSU processome in state pre-A1 shown in different views. (**B**) Multiple focused 3D classifications and refinement strategies used for the reconstruction of sub-modules of the SSU processome in state pre-A1. The maps were further improved with phenix.resolve_cryo_em (Denmod). Reported resolutions from Relion and Denmod are indicated in blue and green, respectively. Masks used for the different classifications and refinements are color-coded and shown in (**A**) or (**B**).

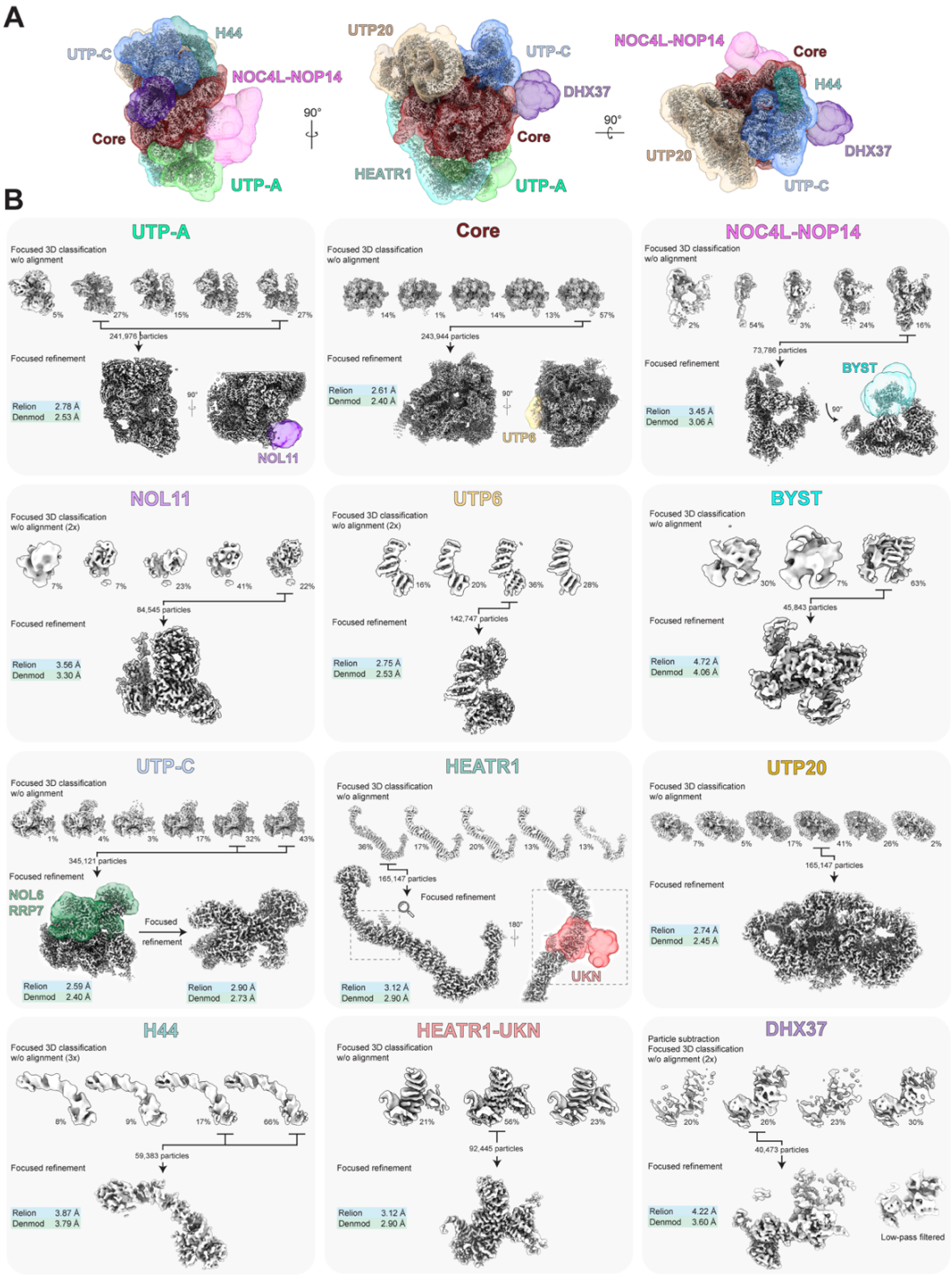

Fig. S5. Cryo-EM processing of state post-A1.

(**A**) Cryo-EM structure of the human SSU processome in state post-A1 shown in different views. (**B**) Multiple focused 3D classifications and refinement strategies used for the reconstruction of sub-modules of the SSU processome in state post-A1. The maps were further improved with phenix.resolve_cryo_em (Denmod). Reported resolutions from Relion and Denmod are indicated in blue and green, respectively. Masks used for the different classifications and refinements are color-coded and shown in (**A**) or (**B**).

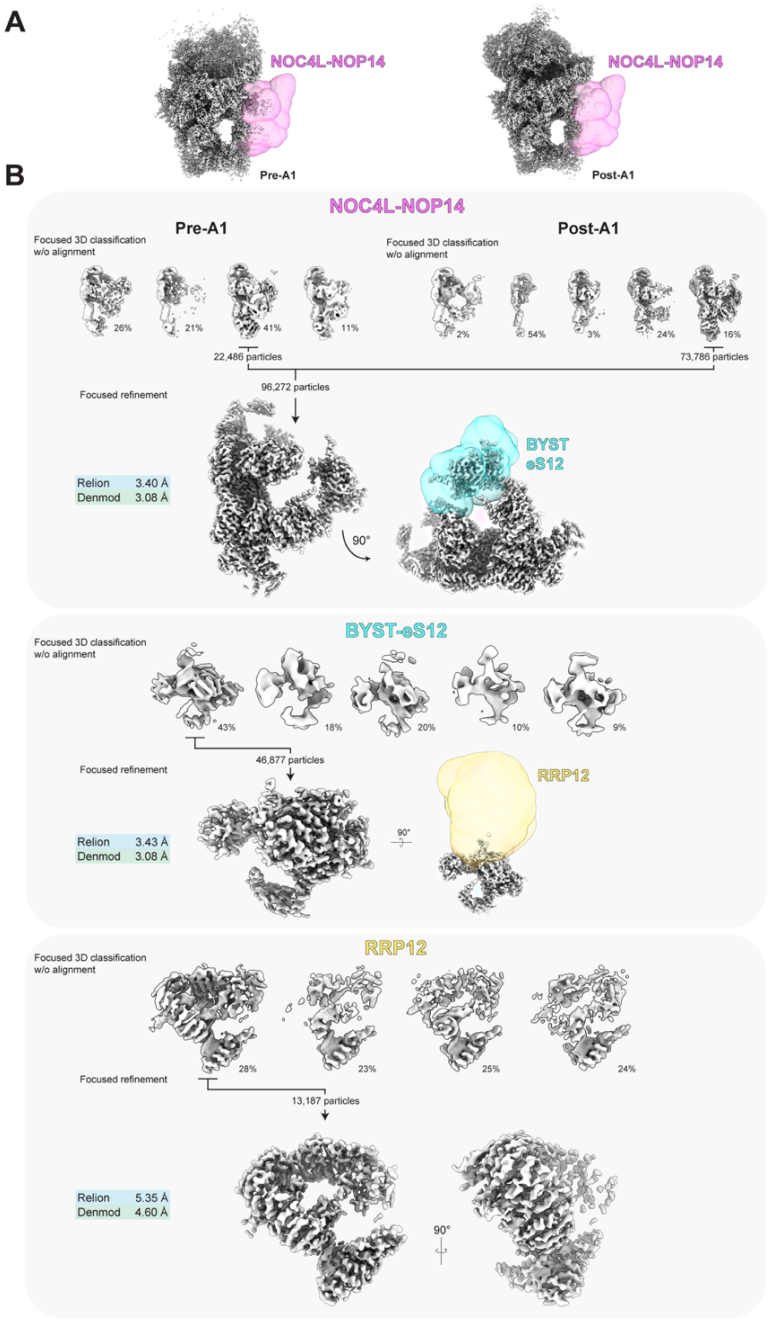

Fig. S6. Cryo-EM processing of elements present in states pre-A1 and post-A1.

(**A**) Cryo-EM structure of the human SSU processome state pre-A1 and post-A1 shown from a side view. (**B**) Focused 3D classification and refinement strategy used for the reconstruction of the NOC4L-NOP14, BYST-eS12 and RRP12 modules. Particles from pre-A1 and post-A1 states were merged to increase the quality and resolution of the reconstruction. The reconstructions were further improved with phenix.resolve_cryo_em (Denmod). Reported resolutions from Relion and Denmod are indicated in blue and green, respectively. Masks used for the different classifications and refinements are color-coded and shown in (**A**) or (**B**).

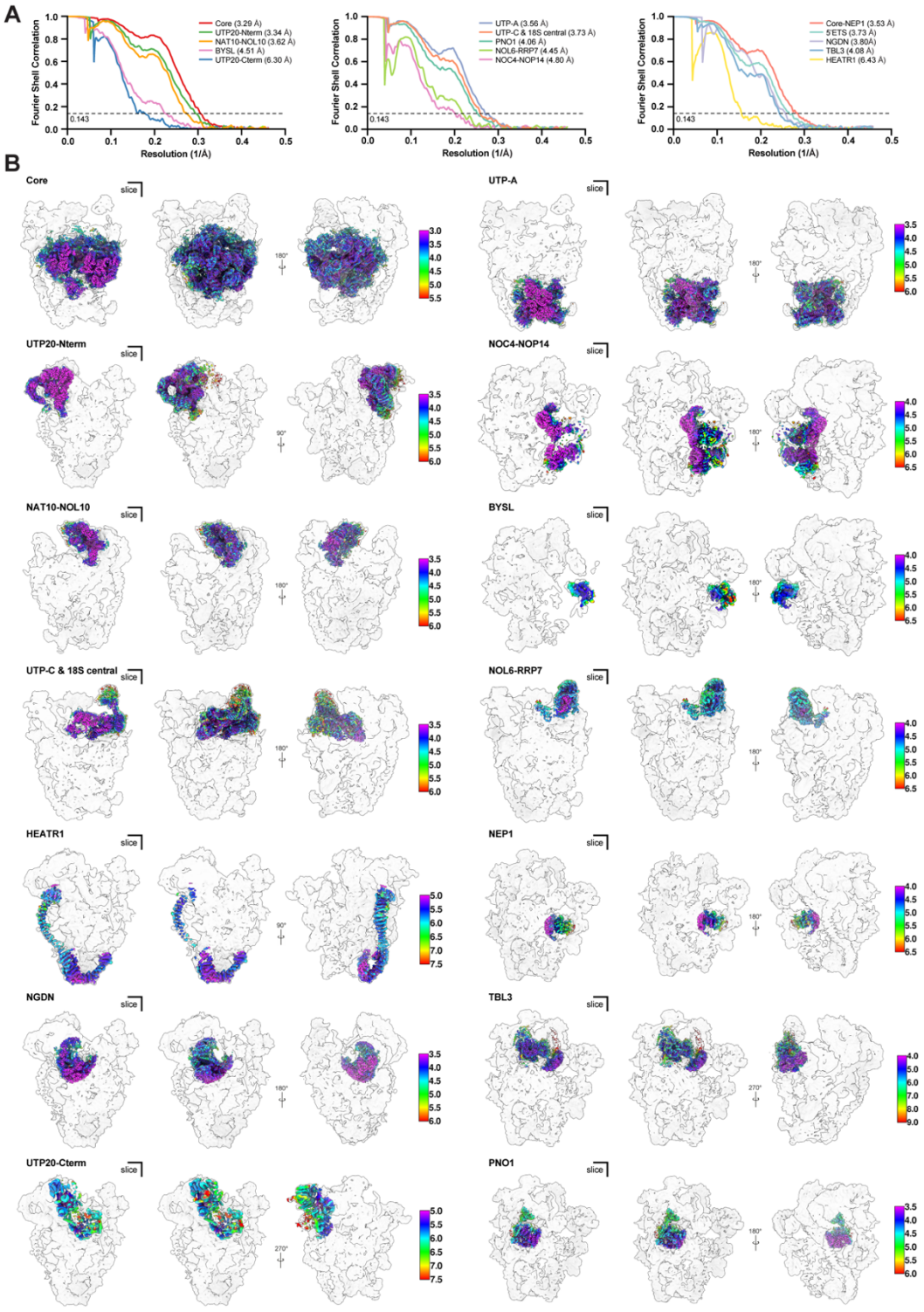

Fig. S7. Local resolution analysis of state pre-A1.

(**A**) Solvent-corrected FSC curves of the different focused refinements. The resolution is indicated for each map and was determined at FSC-0.143 (**B**) Local resolution estimation of the cryo-EM maps from the focused refinements, displayed in their respective location within the SSU processome.

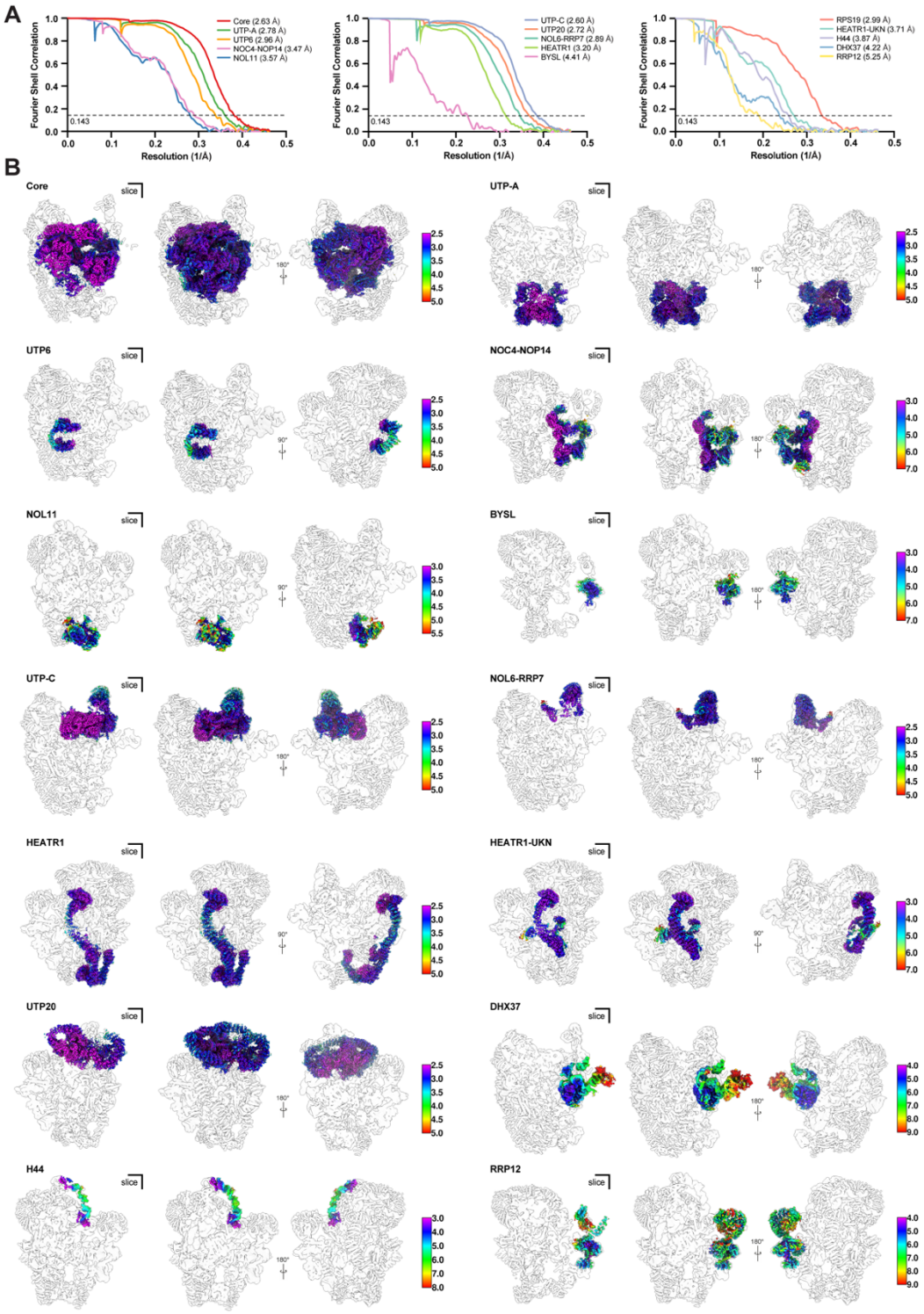

Fig. S8. Local resolution analysis of state post-A1.

(**A**) Solvent-corrected FSC curves of the different focused refinements. The resolution is indicated for each map and was determined at FSC-0.143. (**B**) Local resolution estimation of the cryo-EM maps from the focused refinements, displayed in their respective location within the SSU processome.

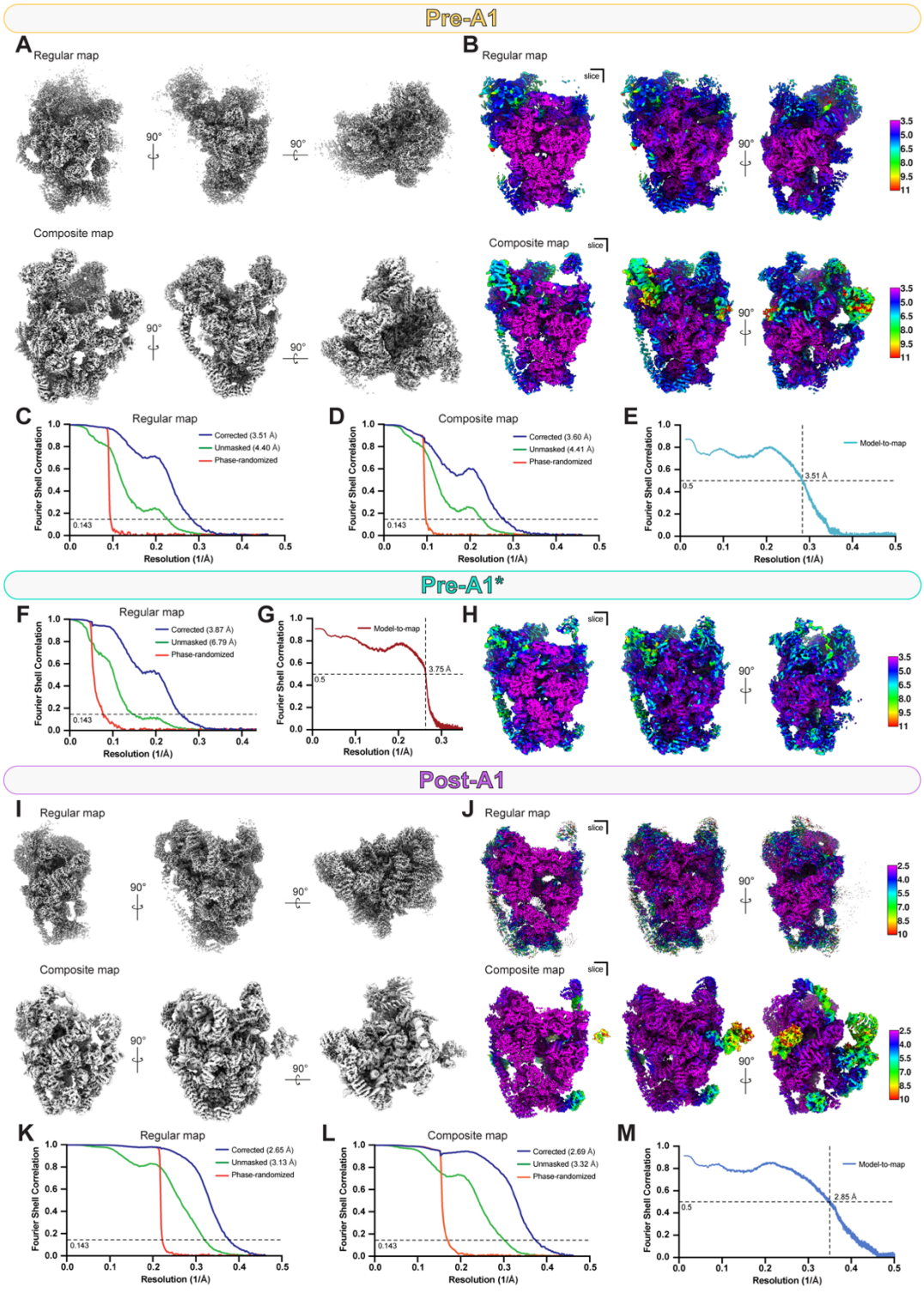

Fig. S9. Cryo-EM map analysis of human SSU processome states.

(**A**) Comparison of the regular cryo-EM reconstruction of human SSU processome state pre-A1 with its composite version. (**B**) Local resolution estimation of the regular and composite EM reconstructions of state pre-A1. (**C, D**) Solvent-corrected and unmasked FSC curves of the regular (C) and composite (D) cryo-EM maps of state pre-A1. (**E**) Map-

to-model FSC curve showing the fit of the overall atomic structure in state pre-A1 with respect to the composite map used for refinement. (**F**) Solvent-corrected and unmasked FSC curve of the human SSU processome in state pre-A1*. (**G**) Map-to-model FSC curve showing the fit of the overall atomic structure in state pre-A1* with respect to the map used for refinement. (**H**) Local resolution estimation of the EM reconstruction of state pre-A1*. (**I**) Comparison of the regular cryo-EM reconstruction of human SSU processome in state pre-A1 with its composite version. (**J**) Local resolution estimation of the regular and composite EM reconstructions of state post-A1. (**K, L**) Solvent-corrected and unmasked FSC curves of the regular (K) and composite (L) cryo-EM maps of state post-A1. (**M**) Map-to-model FSC curve showing the fit of the overall atomic structure in state post-A1 with respect to the composite map used for refinement.

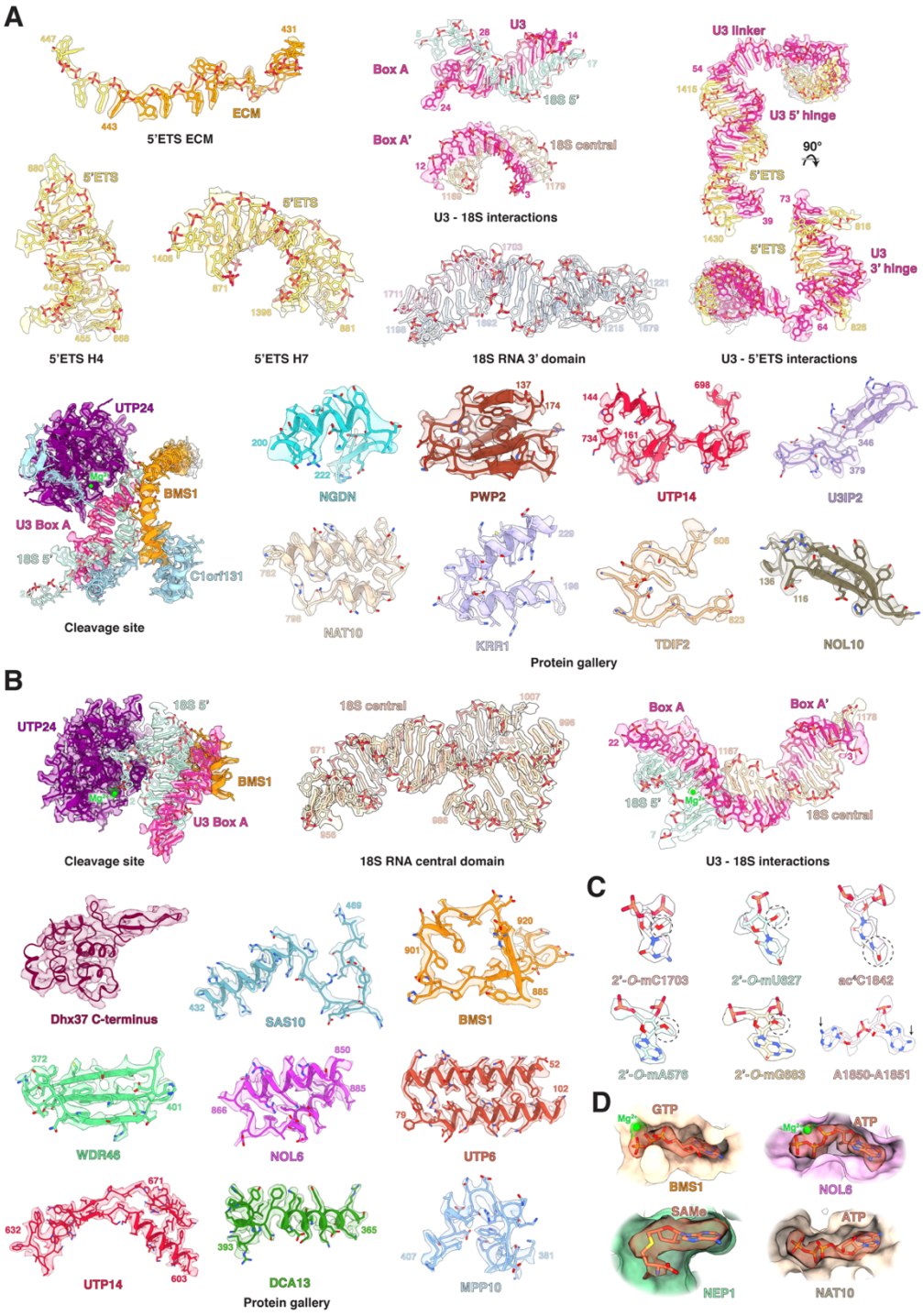

Fig. S10. Representative cryo-EM densities.

Selection of representative densities for assembly factors and RNAs present in (**A**) state pre-A1 and (**B**) state post-A1. (**C**) Modified RNA bases displayed in their respective EM densities with C1842 acetylated by NAT10 and A1850-1851 not yet modified by DIM1. The arrows indicate that A1850-A1851 are not modified. (**D**) Nucleotides and co-factors bound to assembly factors displayed in their respective EM densities. Densities are illustrated as continuous transparent volumes and models are shown as ribbons and sticks.

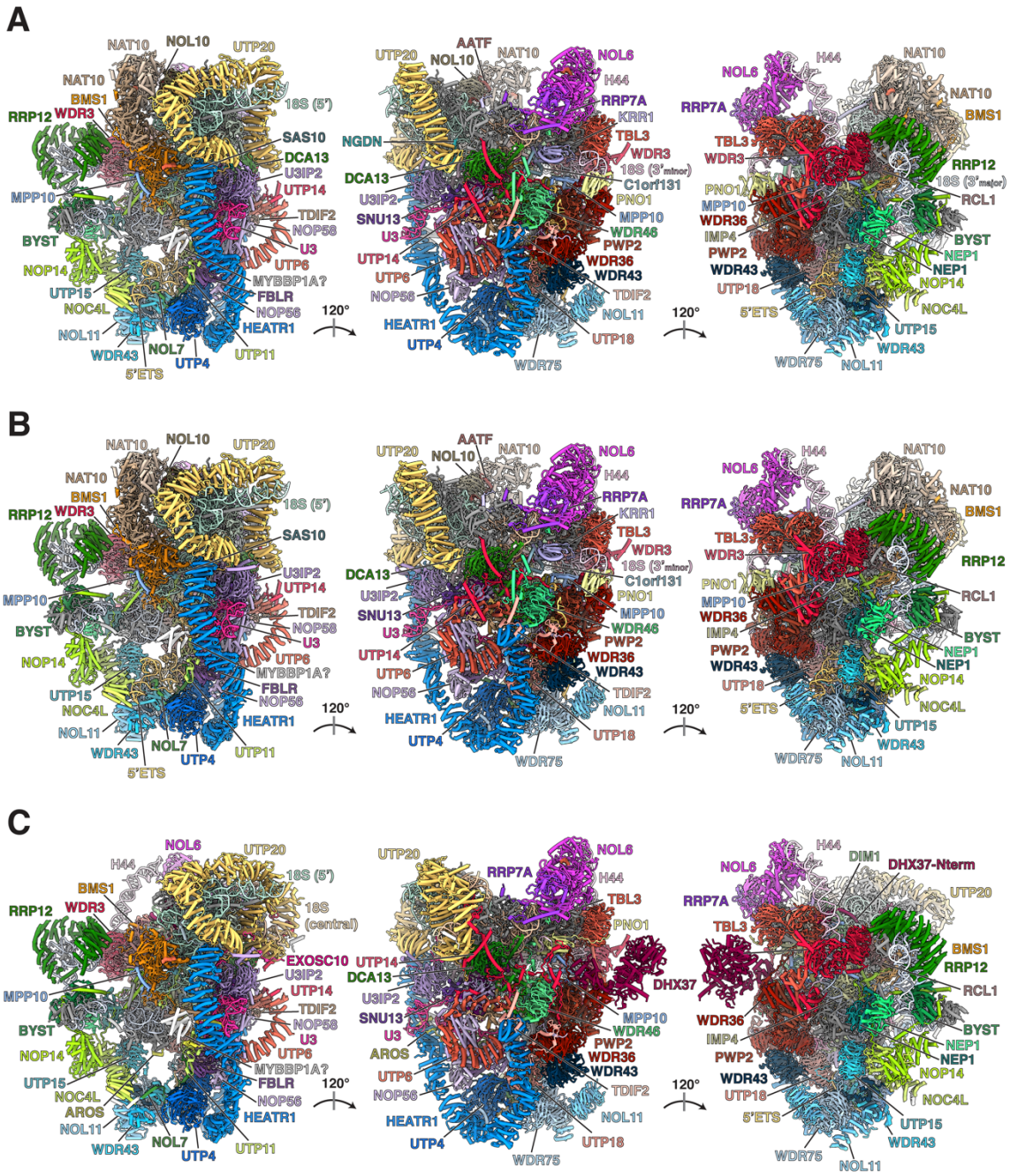

Fig. S11. Nucleolar maturation of human SSU processomes.

Three states of the human SSU processome in different views with labeled assembly factors. (**A**) pre-A1 (**B**) pre-A1* and (**C**) post-A1

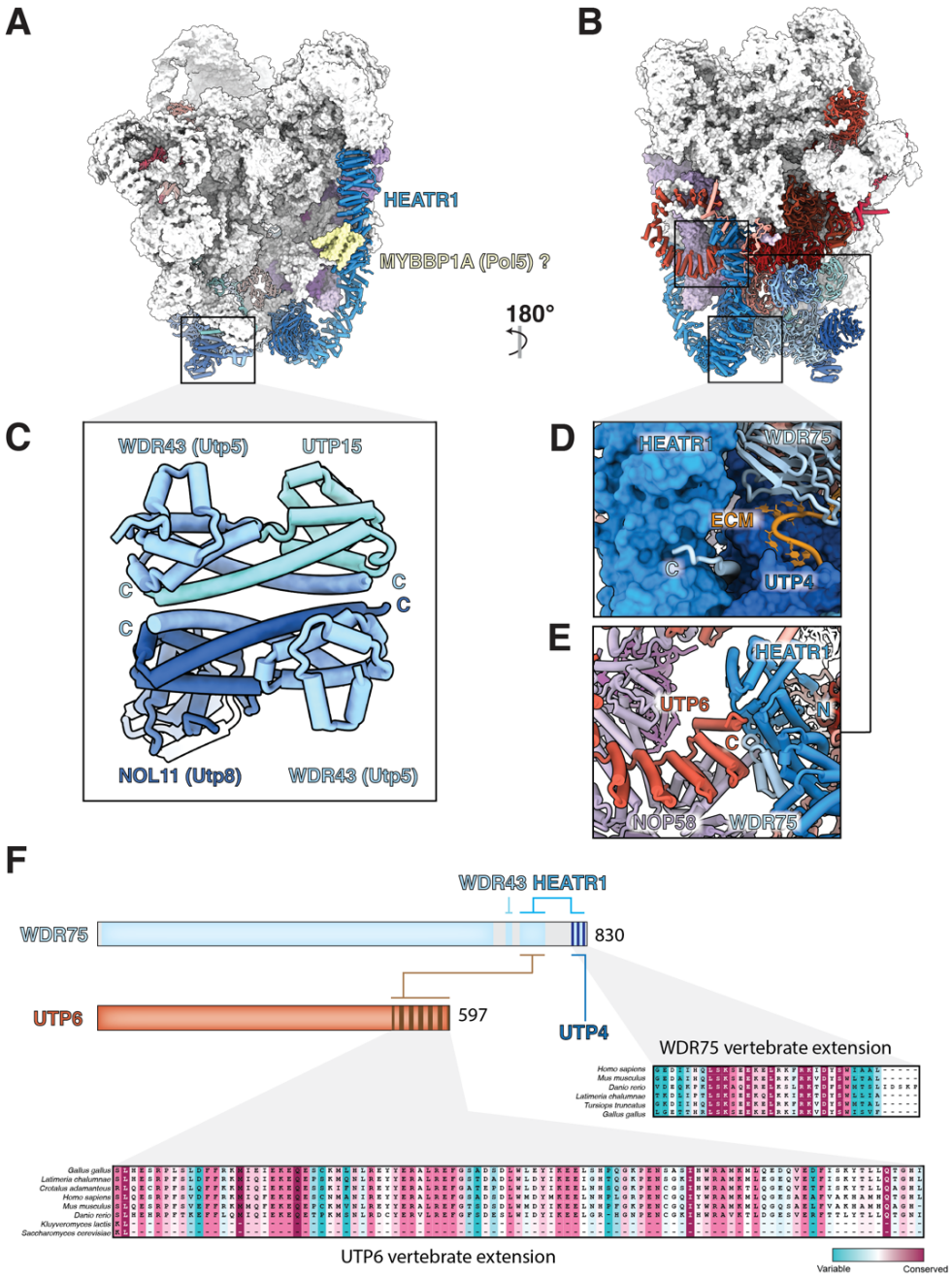

Fig. S12. Vertebrate adaptations of UtpA and UtpB.

(**A, B**) Two views of the human SSU processome in state post-A1 with UtpA, UtpB, and the U3 snoRNP colored in shades of blue, red and purple respectively. A tentatively assigned protein (MYBBP1A/Pol5) is indicated in yellow. (**C**) Detailed view of the tetramerization module of human UtpA that involves two copies of WDR43 (Utp5 in yeast). (**D, E**) Vertebrate-specific extensions of the C-termini of WDR75 (D) and UTP6, which recognizes the HEATR1/WDR75 complex (E). (**F**) Schematic illustrations of WDR75 and UTP6 and their interaction partners. Vertebrate-specific extensions of WDR75 and UTP6 are highlighted with darker shaded bars and corresponding multiple sequence alignments for these regions.

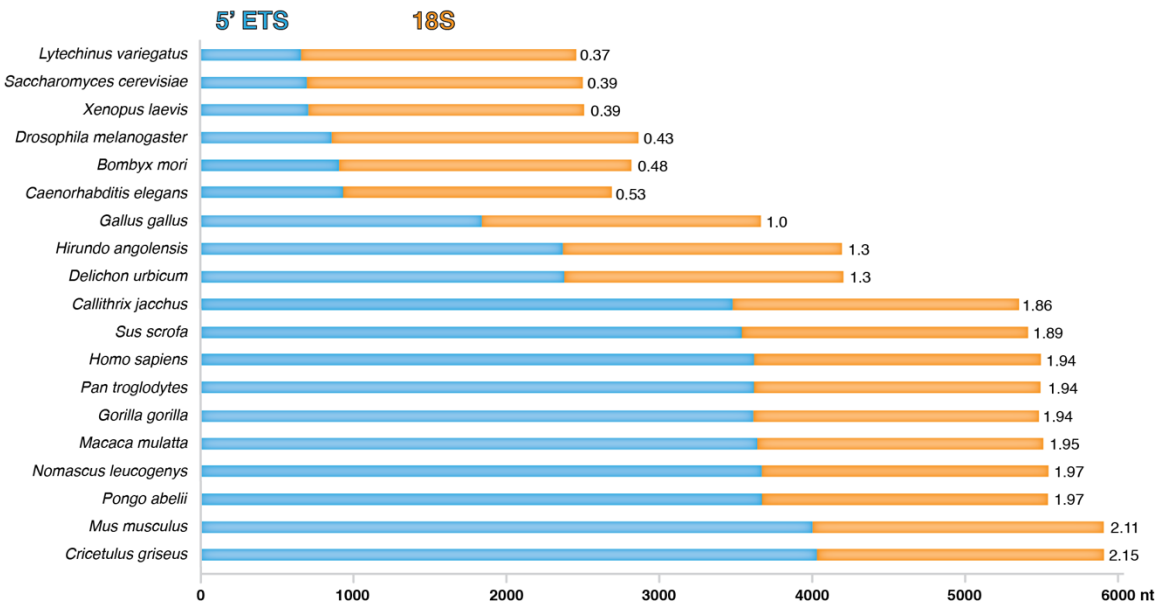

Fig. S13. Evolutionary expansion of the 5' external transcribed spacer.

Bar chart representing the length in nucleotides (nt) of the 5' external transcribed spacer (5' ETS; blue) versus mature 18S rRNA (orange) in different eukaryotic species. The ratio for each species (blue/orange) is denoted at the end of its respective bar.

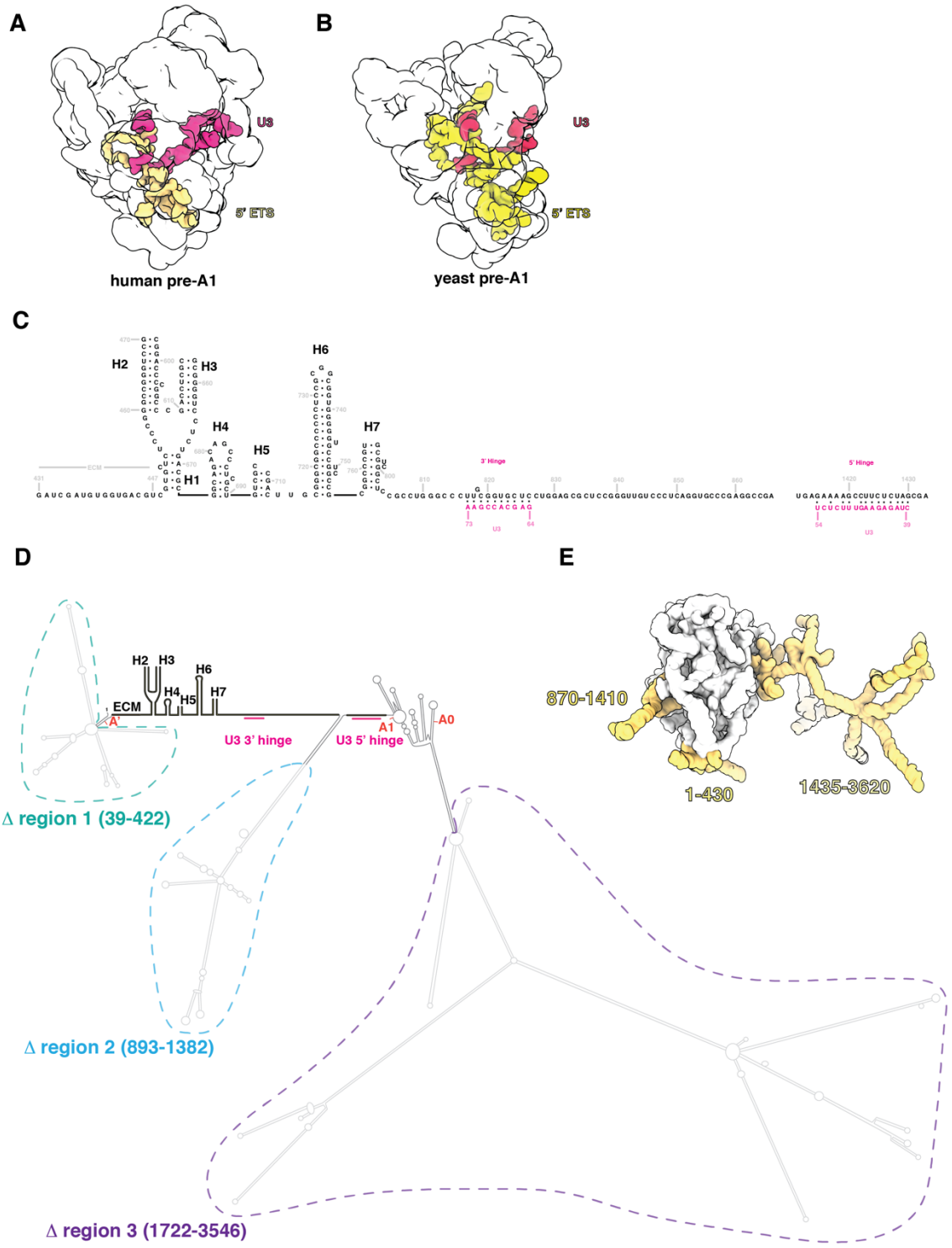

Fig. S14. Architecture and truncations of the human 5' ETS.

(**A, B**) Architectural views of human (A; this study) and yeast (B; PDB 5WLC) SSU processomes in state pre-A1 with 5' ETS (shades of yellow) and U3 snoRNA (shades of red/pink) shown. (**C**) Sequence and secondary structure of the built 5' ETS sequence in the human pre-A1 model (black) with base pairing U3 3' and 5' hinges (pink). (**D**) Secondary

structure of the full-length human 5' ETS rRNA with cleavage sites (A', A0 and A1; red) and U3 snoRNA binding regions (pink) shown. Sections (regions 1-3) that are truncated in functional studies are indicated by color-coded dashed lines. (**E**) Architectural view of the human SSU processome with a putative 3D model for the entire 5' ETS. Putative secondary structures for flexible regions (D) were obtained using the ViennaRNA package (*75*) and corresponding 3D models (E) were obtained using RNAcomposer (*76*).

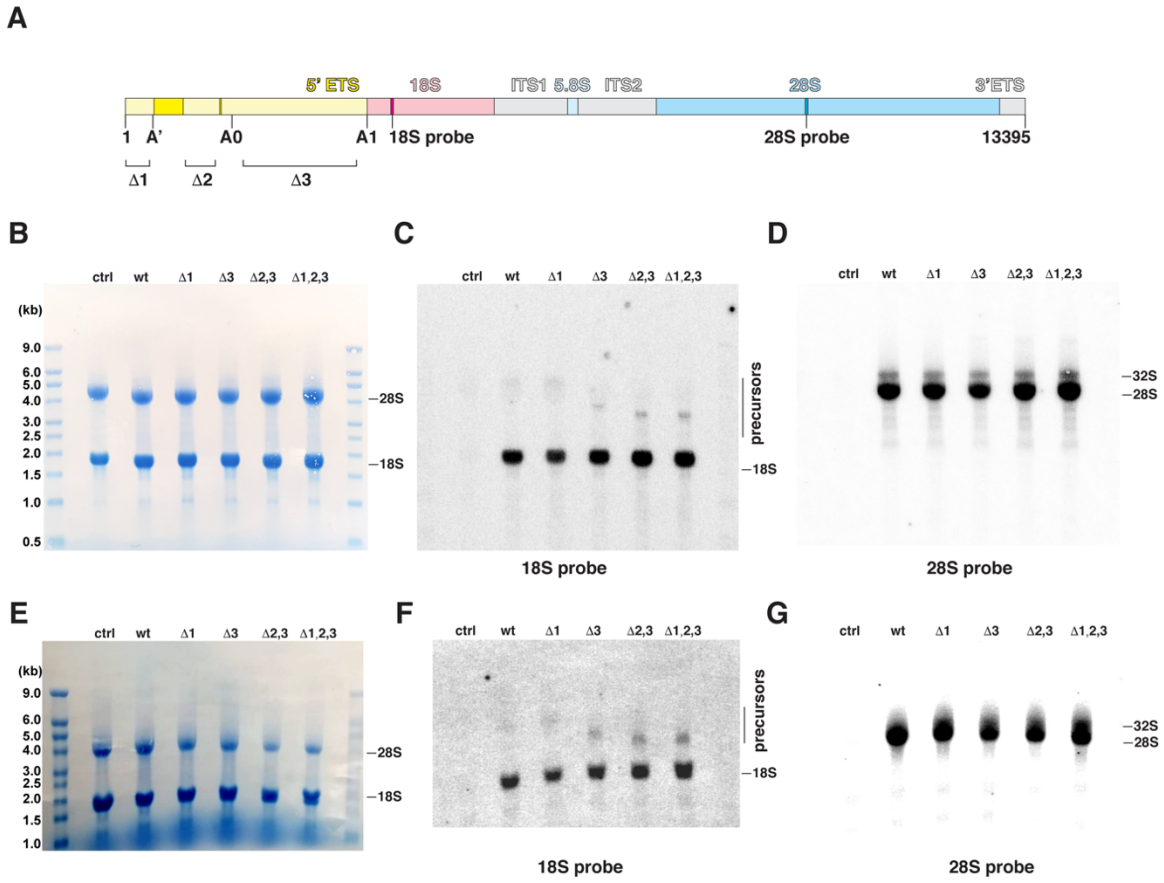

Fig. S15. Functional studies of recombinant human rDNA loci.

(**A**) Schematic representation of a human ribosomal RNA transcript showing truncations (Δ1, Δ2, Δ3) within the 5' external transcribed spacer (5' ETS). Unique sequences inserted in the 18S and 28S transcripts can be recognized by the 18S probe and 28S probe, respectively. (**B**) Methylene blue staining showing 18S and 28S RNA bands detected from a non-transfected control (ctrl), or cells transfected with wild-type (wt, full-length rDNA plasmid) or four plasmids harboring truncations (Δ1, Δ3, Δ2,3 and Δ1,2,3). (**C**) Northern blot analysis using the 18S probe showing bands corresponding to the mature 18S rRNA and its precursors (black line). (**D**) Northern blot analysis using the 28S probe showing bands corresponding to the mature 28S rRNA and its precursor, the 32S pre-rRNA. (**E, F, G**) Biological replicate of (B, C, D).

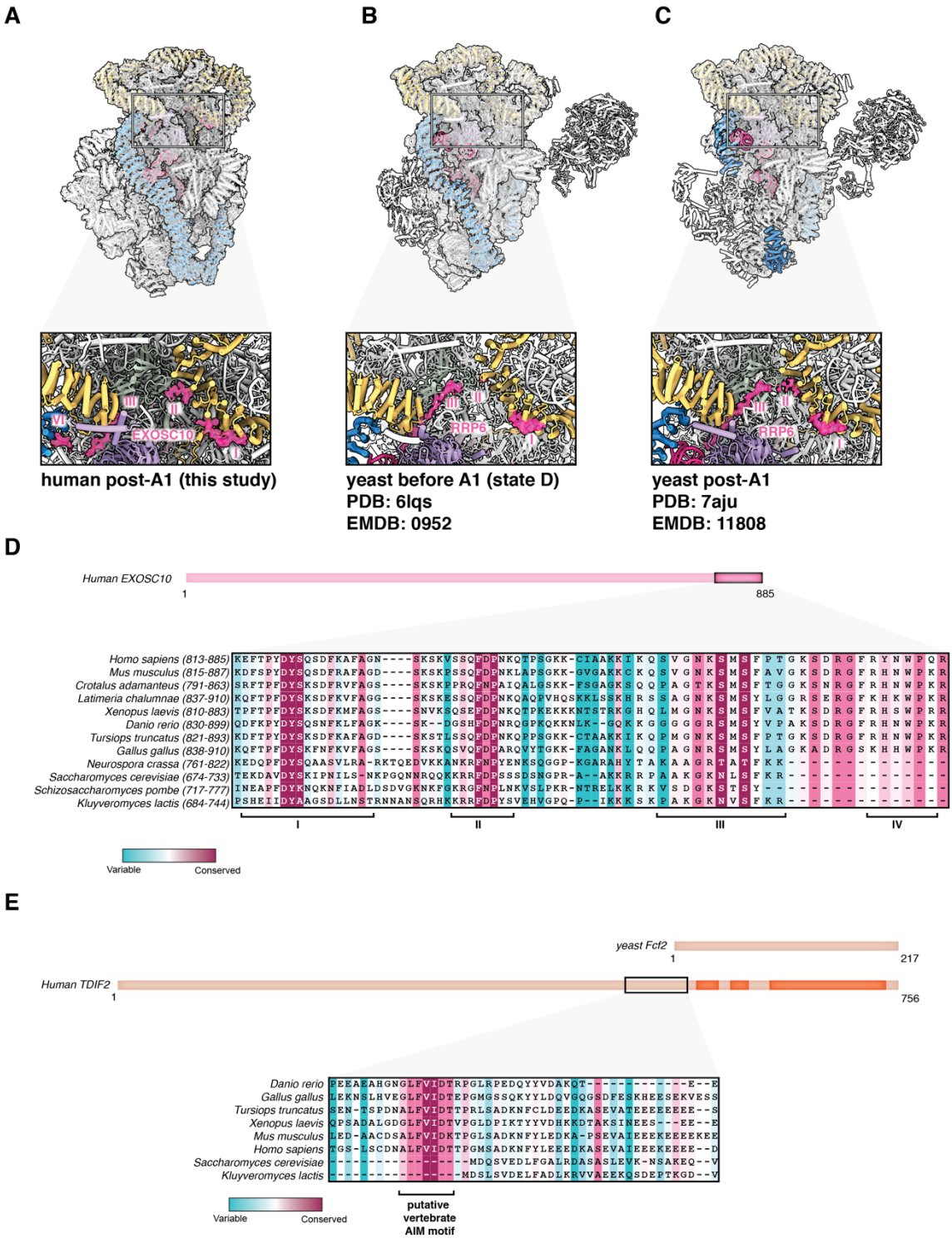

Fig. S16. Mechanisms of licensing for exosome-mediated SSU processome maturation.

(**A**) The structure of the human post-A1 SSU processome highlighting the exosome-associated nuclease EXOSC10 and its interaction partners. The "lasso" region of EXOSC10 (pink atomic model and density) recognizes the human SSU processome in the

post-A1 state via four peptide motifs (I – IV). (**B, C**) Structures of the exosome-bound yeast SSU processomes before (state D; panel B) or after cleavage at site A1 (state post-A1; panel C) with identified difference density corresponding to Rrp6 shown in pink. (**D**) Multiple sequence alignment of the human EXOSC10 "lasso" region and homologs highlighting universal presence of peptide motifs I-III and vertebrate-specific presence of motif IV. (**E**) Schematic comparison of yeast Fcf2 and human TDIF2. Darker shades of orange indicate built segments of TDIF2. A black box denotes the location of the putative human AIM motif. Multiple sequence alignment of a region in human TDIF2 containing a putative vertebrate-specific AIM motif.

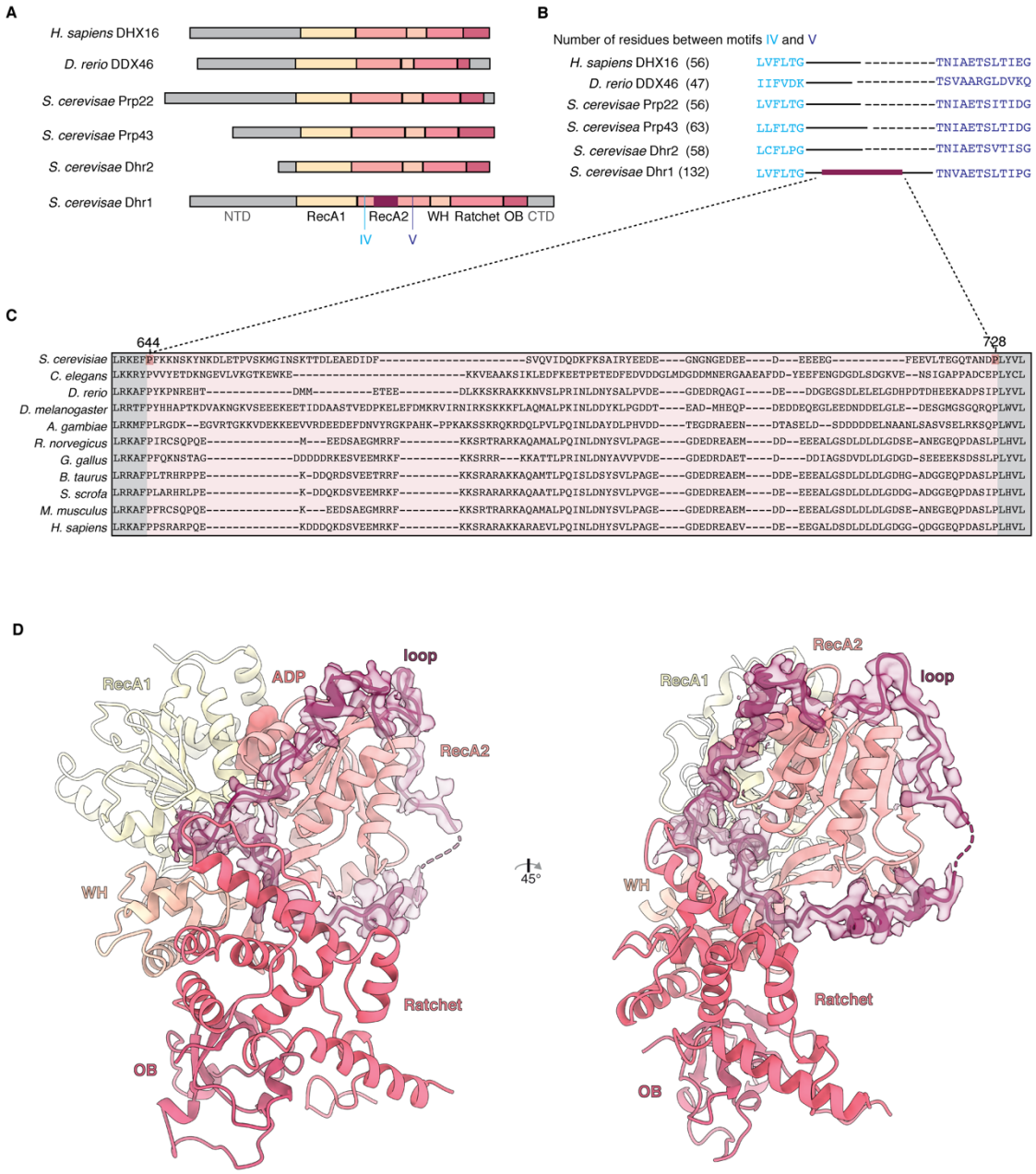

Fig. S17. Structural analysis of Dhr1.

(**A**) Comparison of DEAH-box helicases highlights the presence of a Dhr1-specific loop in the RecA2 domain between motifs IV and V. (**B**) Analysis of sequence lengths between motifs IV and V in DEAH-box helicases. (**C**) Multiple sequence alignment of the auto-inhibitory loop with Dhr1 enzymes. (**D**) Two views of the yeast Dhr1 core with density corresponding to the auto-inhibitory loop shown.

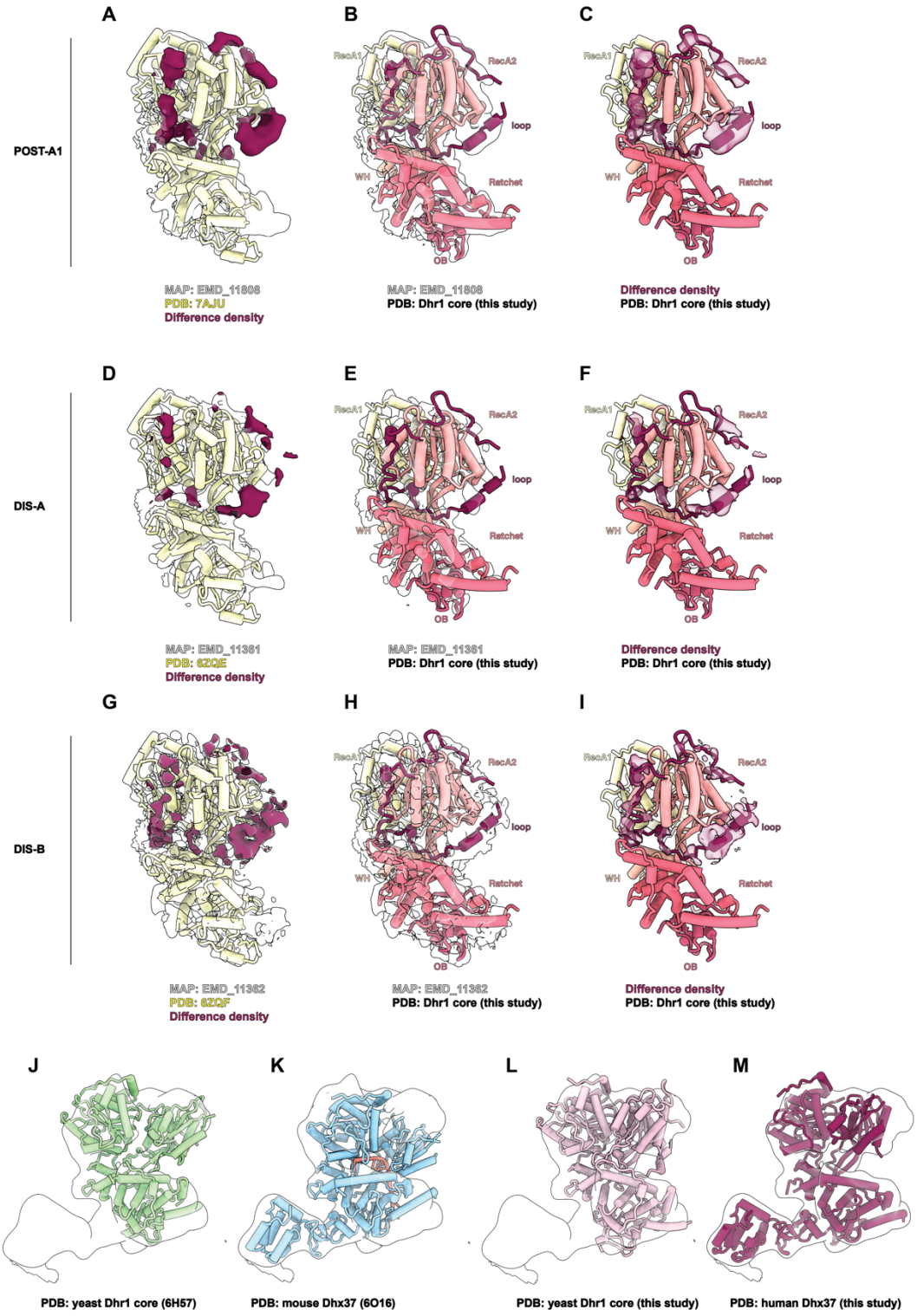

Fig. S18. Auto-inhibition of the DEAH-box helicase Dhr1/Dhx37.

(**A-C**) Analysis of Dhr1 in the yeast SSU processome state post-A1. (**A**) Original model (yellow) and map (transparent) as well as difference density (map vs model; dark red) are shown. (**B**) Dhr1 core structure (this study) docked in the yeast SSU processome state post-

A1. (**C**) Dhr core structure (this study) shown with difference density from panel A. (**D-F**) Analysis of Dhr1 in the yeast SSU processome state DIS-A. (**D**) Original model (yellow) and map (transparent) as well as difference density (map vs model; dark red) are shown. (**E**) Dhr1 core structure (this study) docked in the yeast SSU processome state DIS-A. (**F**) Dhr core structure (this study) shown with difference density from panel D. (**G-I**) Analysis of Dhr1 in the yeast SSU processome state DIS-B. (**G**) Original model (yellow) and map (transparent) as well as difference density (map vs model; dark red) are shown. (**H**) Dhr1 core structure (this study) docked in the yeast SSU processome state DIS-B. (**I**) Dhr core structure (this study) shown with difference density from panel G. (**J-M**) Fitting of Dhr1 structures into the human SSU processome in state post-A1 (this study) with yeast apo Dhr1 core (PDB 6H57, **J**), RNA-bound mouse DHX37 (**K**), yeast Dhr1 core (this study, **L**) and human DHX37 (this study, **M**).

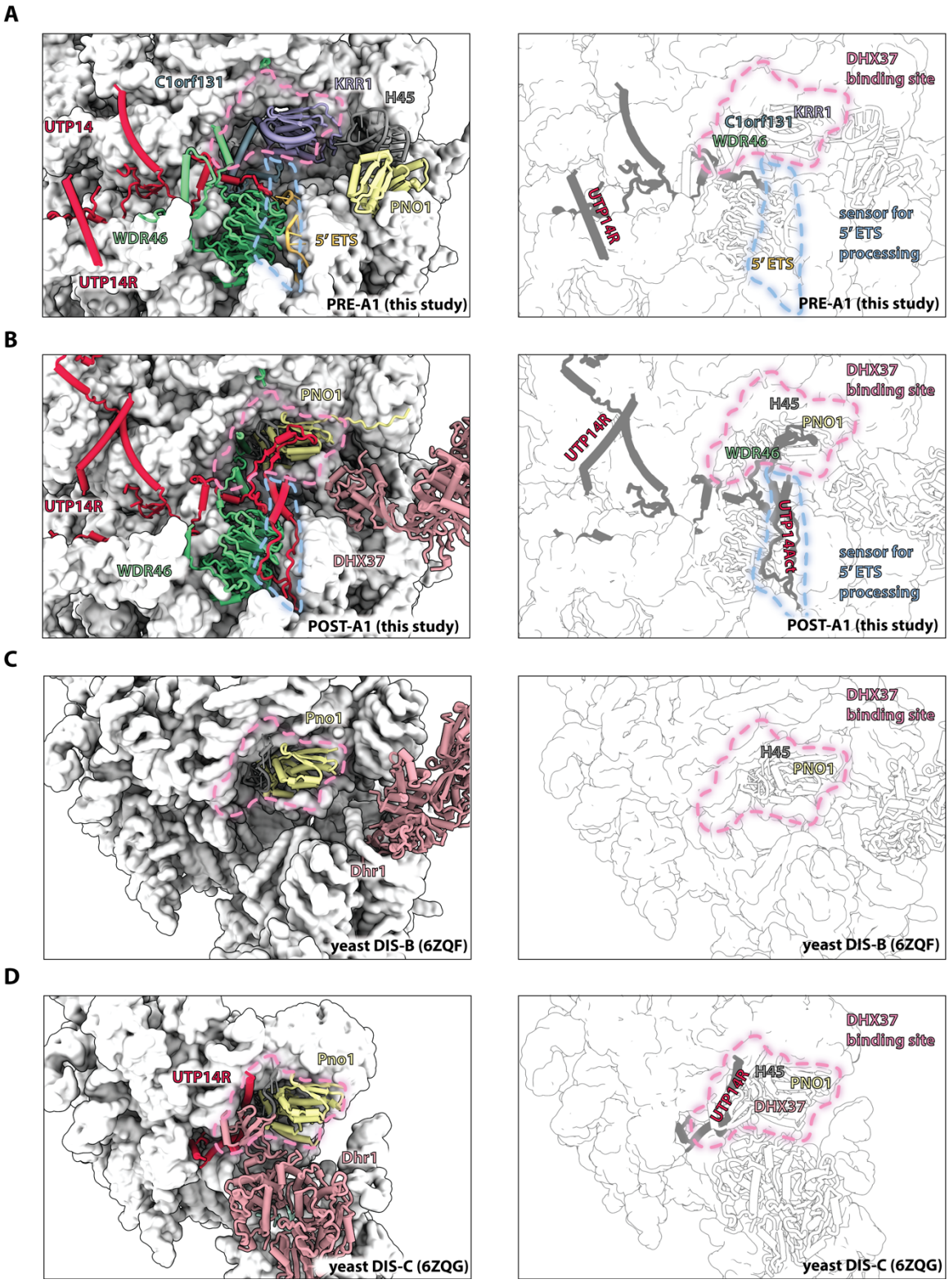

Fig. S19. Molecular control of UTP14 and DHX37.

Chronology of structural changes in the maturation of the SSU that control DHX37 activity and localization. Left Panels: Models of pre-ribosomal particles displaying factors

involved in DHX37 regulation. The DHX37 binding site and the sensor for 5' ETS processing are demarcated with dashed lines in pink and blue respectively. Right panels: Simplified schematics showing major structural changes with respect to the DHX37 binding site (dashed pink line) (**A**) Human state pre-A1, (**B**) Human state post-A1, (**C**) yeast DIS-B (PDB: 6ZQF), and (**D**) yeast DIS-C (PDB: 6ZQG).

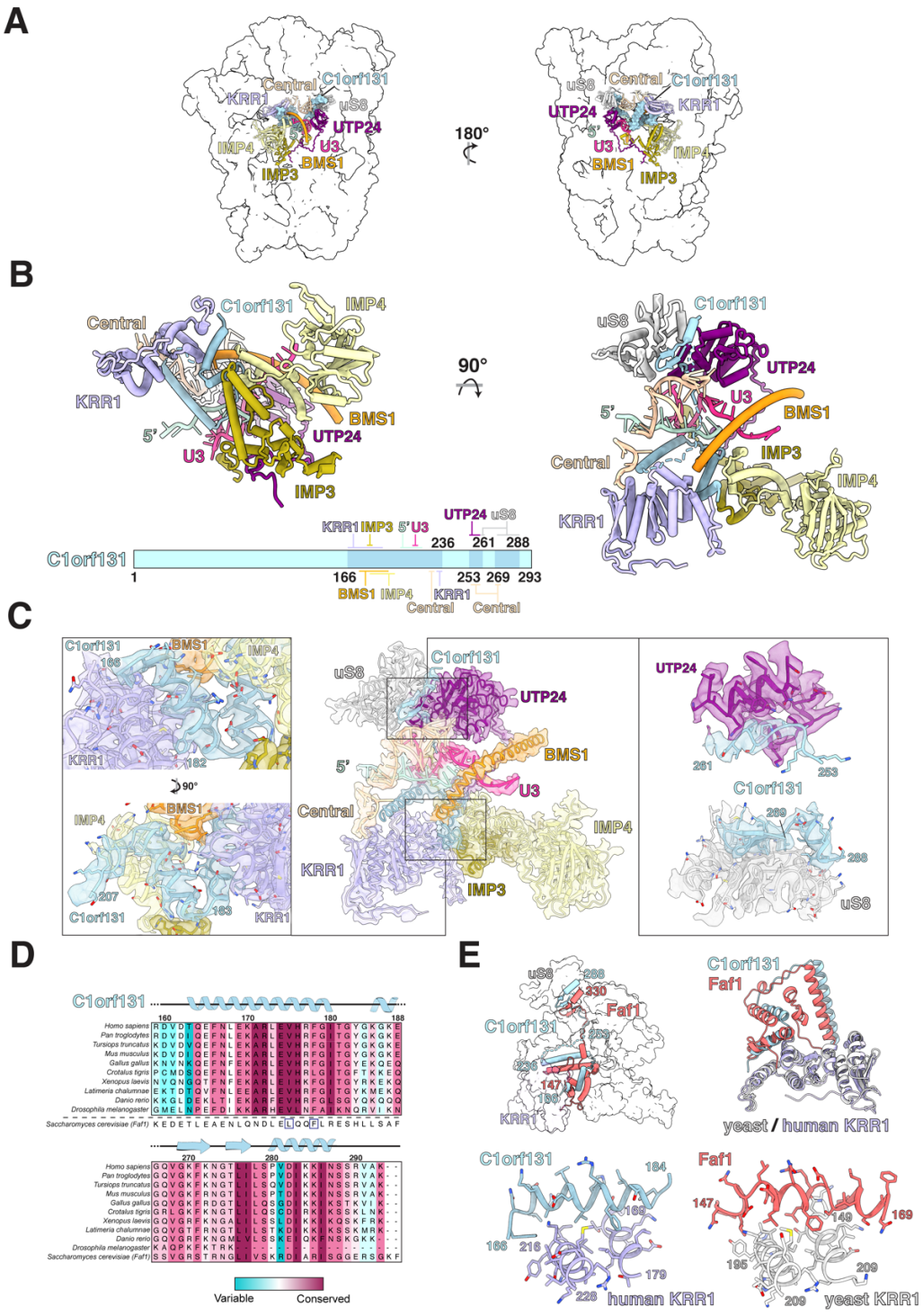

Fig. S20. Functional architecture of C1orf131.

(**A**) Location of C1orf131 and proximal proteins and RNAs within state pre-A1. (**B**) Two views of C1orf131 and the cluster of neighboring proteins and RNA. A schematic of C1orf131 (cyan) highlights ordered regions (blue) and their interaction partners. (**C**) Detailed views highlighting the interactions between C1orf131 and KRR1 (left) and UTP24 and uS8 (right). Proteins and corresponding densities for all factors are color-

coded. (**D**) Multiple sequence alignments and secondary structures of the segments of C1orf131 interacting with KRR1 (top) and uS8 (bottom). The sequence of yeast homolog Faf1 is shown below. (**E**) Top: Comparisons of the topology of human C1orf131 (cyan, within state pre-A1) and yeast Faf1 (red, PDB: 6ke6). Bottom: Comparison of the interface between human KRR1-C1orf131 (left) and yeast Krr1-Faf1 (right).

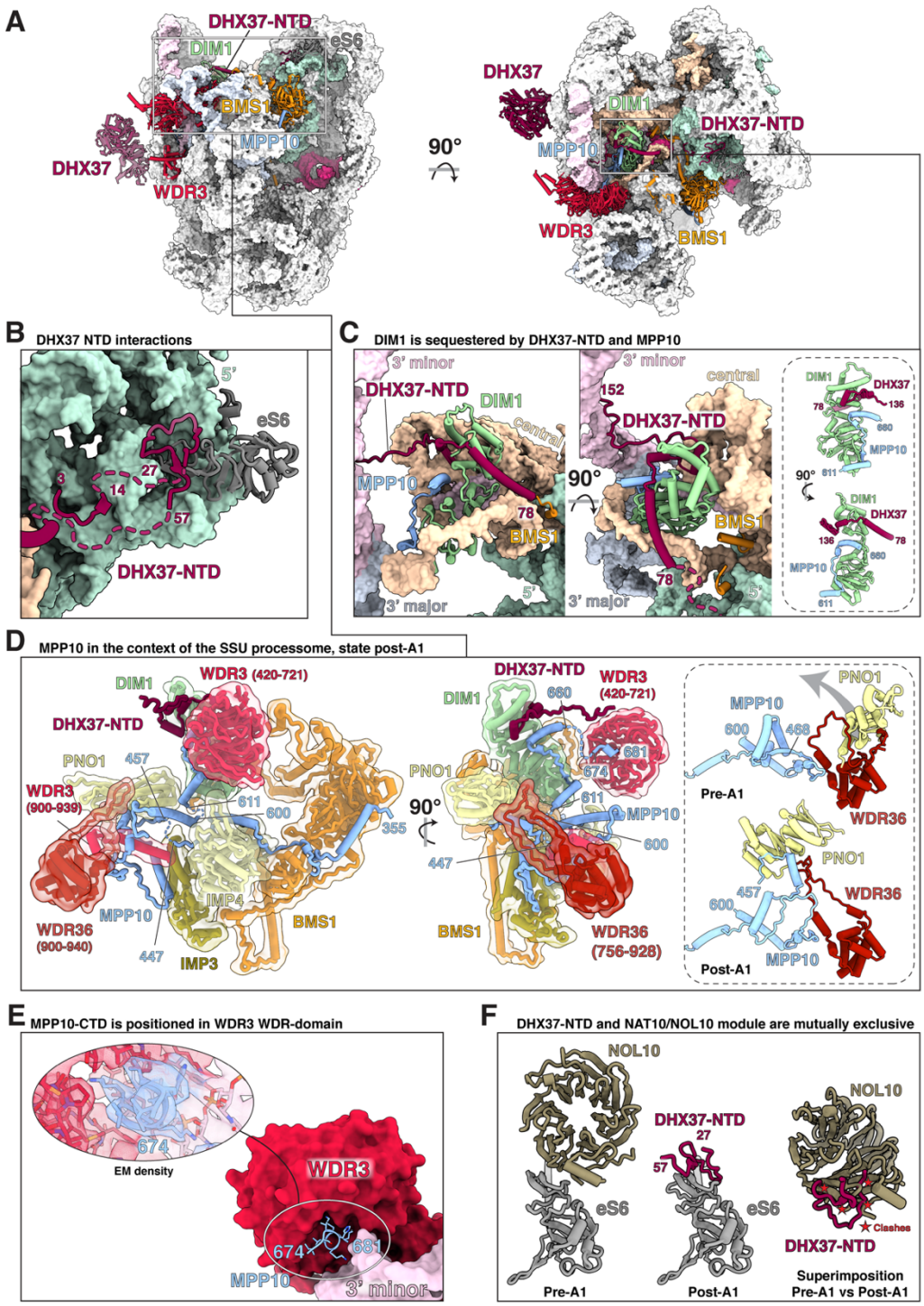

Fig. S21. Interactions of MPP10 and DHX37 with DIM1.

(**A**) Two views of the human SSU processome in state post-A1 highlighting DHX37, DIM1 and MPP10 and their interaction partners. (**B**) Detailed view of the interactions between DHX37-NTD (maroon) with eS6 (grey) on top of 18S rRNA (green surface). (**C**) Detailed views showing the sequestration of Dim1 (light green) by MPP10 (blue) and DHX37-NTD (maroon). (**D**) Left: Two related views of the architecture and interactions of MPP10 within

the SSU processome (post-A1). Right inset: Topological changes of MPP10, WDR36 and PNO1 from state pre-A1 (top) to post-A1 (bottom). (**E**) MPP10 (blue, ribbon) residues that bind WDR3 (red surface). Cryo-EM density of the WDR3-MPP10 interface is shown in the zoomed-in view. (**F**) Mutually exclusive binding of NOL10 (left) and DHX37-NTD (center) with eS6. Superposition of DHX37-NTD and NOL10 highlights clashes denoted by red stars (right).

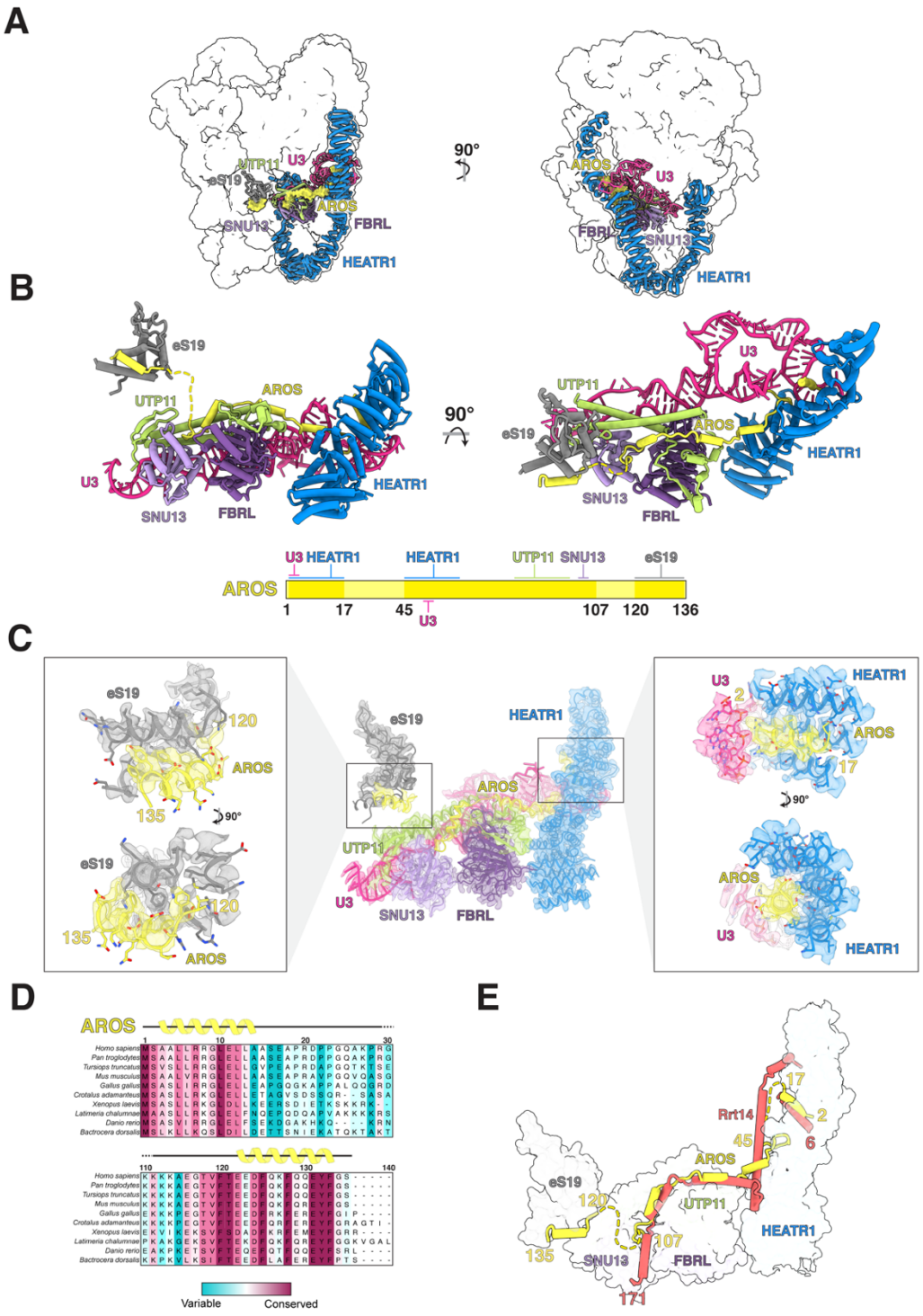

Fig. S22. Functional architecture of AROS.

(**A**) Two views of the location of AROS and its interaction partners within the human SSU processome in state post-A. (**B**) Two views of AROS and the cluster of neighboring factors. A schematic of AROS (light yellow) contains regions built in the post-A1 structure (yellow) and binding sites of assembly factors and U3 snoRNA. (**C**) Detailed views showing the C-terminus of AROS binding to eS19 (left) and the N-terminus of AROS

binding to HEATR1 and U3 snoRNA (right). (**D**) Multiple sequence alignments and secondary structures of N- and C-terminal regions of AROS visualized in (C). (**E**) Comparison of the trajectories of human AROS (within state post-A1) and yeast Rrt4 (PDB: 6lqs).

Map	EMDB ID	Resolution (FSC-0.143 criterion)	Particles (no.)	Applied B-factor	Details
State pre-A1					
5'ETS	EMD-24149	3.73	24,598	-47.60	Focused 3D classification followed by focused refinement
CORE	EMD-24150	3.29	37,758	-39.23	Focused 3D classification followed by focused refinement
HEATR1	EMD-24151	6.37	25,442	-143.41	Focused 3D classification followed by focused refinement
NAT10-NOL10	EMD-24152	3.67	30,201	-56.47	Focused 3D classification followed by focused refinement
NEP1	EMD-24153	3.54	23,684	-42.80	Focused 3D classification followed by focused refinement
NGDN	EMD-24154	3.83	21,770	-25.00	Focused 3D classification (2x) followed by focused refinement
PNO1	EMD-24155	4.06	33,669	-25.00	Focused 3D classification followed by focused refinement
TBL3	EMD-24156	4.09	25,967	-80.30	Focused 3D classification followed by focused refinement
UTP20-CTD	EMD-24157	6.30	12,891	-50.00	Focused 3D classification followed by focused refinement
UTP20-NTD	EMD-24158	3.42	42,746	-62.88	Focused 3D classification followed by focused refinement
UTPA	EMD-24159	3.58	26,589	-53.11	Focused 3D classification followed by focused refinement
UTPC	EMD-24160	4.45	26,376	-96.75	Focused 3D classification followed by focused refinement
UTPC-Central	EMD-24161	3.73	26,376	-56.13	Focused 3D classification followed by focused refinement
Overall pre-A1	EMD-23939	3.51	42,142	-44.44	Overall 3D refinement
Composite pre-A1	EMD-23936	3.60			Composite map generated with all pre-A1 and merged states focused maps using phenix.combine_focused_maps
State post-A1					
CORE	EMD-24162	2.63	243,944	-38.29	Focused 3D classification followed by focused refinement
DHX37	EMD-24163	4.23	40,473	0.00	Signal subtraction, Focused 3D classification (2x), signal revert followed by focused refinement
H44	EMD-24164	3.87	59,383	-50.00	Focused 3D classification (3x) followed by focused refinement
HEATR1	EMD-24165	3.2	165,147	-66.58	Focused 3D classification followed by focused refinement
NOL11	EMD-24166	3.57	84,545	-40.00	Focused 3D classification (2x) followed by focused refinement
Probable MYBBP1A	EMD-24167	3.71	92,445	-60.00	Focused 3D classification followed by focused refinement
RPS19-AROS	EMD-24168	2.99	83,167	-44.45	Focused 3D classification followed by focused refinement
UTP20	EMD-24169	2.72	190,960	-43.51	Focused 3D classification followed by focused refinement
UTP6	EMD-24170	2.96	142,747	-39.85	Focused 3D classification (2x) followed by focused refinement
UTPA	EMD-24171	2.78	241,976	-48.34	Focused 3D classification followed by focused refinement

Description	EMDB ID	Resolution (FSC-0.143 criterion)	Particles (no.)	Applied B-factor	Details
UTPC	EMD-24172	2.89	345,121	-61.37	Focused 3D classification followed by focused refinement
UTPC-Central	EMD-24173	2.6	345,121	-46.68	Focused 3D classification followed by focused refinement
Overall post-A1	EMD-23940	2.65	459,775	-47.02	Overall 3D refinement
Composite post-A1	EMD-23938	2.69			Composite map generated with all post-A1 and merged states focused maps using phenix.combine_focused_maps
Merged states					
BYST-RPS12	EMD-24174	3.46	62,895	-62.37	Focused 3D classification, merging of particles followed by focused refinement
NOC4L-NOP14	EMD-24175	3.41	107,006	-64.82	Focused 3D classification, merging of particles followed by focused refinement
RRP12-BYST	EMD-24176	5.25	23,288	-60.00	Focused 3D classification, merging of particles followed by focused refinement

Table S1. Focused, overall and composite maps statistics.

Subcomplex	Chain ID	SegID	Molecule name (human/yeast)	Total residues or bases	Domains	Modelled (residues range)	Modeling template	Modeling method	Maps used for building
RNA	L0	L0	5'ETS rRNA	3620		atomic (431-447)		Manual building	UTP-A map
	L1	L1	pre-18S rRNA	1880		atomic (2-135, 140-196, 203-240, 246-251, 268-628, 635-655, 660-708, 720-756, 788-835, 840-868, 901-1237, 1265-1323, 1326-1341, 1345-1359, 1364-1400, 1446-1503, 1510-1516, 1520-1552, 1560-1575, 1588-1616, 1623-1692, 1696-1826, 1839-1872, +62 Mg^{2+})	5WLC/6ZQD/6ZOJ	Docked & rebuilt	Core, UTP-C & H44 maps
	L2	L2	U3 snoRNA	217		atomic (3-22,29-40,73-217)	5WLC/6ZQD	Docked & rebuilt	Core map
Ribosomal proteins	L3	L3	S18/S18 (uS13)	152		atomic (3-87), poly-A (88-116)	6ZOJ	Docked & adjusted	Core map
	L4	L4	S4X/S4 (eS4)	263		atomic (2-263)	6ZOJ	Docked & adjusted	Core map
	L5	L5	S5/S5 (uS7)	204		atomic (15-204)	6ZOJ	Docked & adjusted	Core map
	L6	L6	S6/S6 (eS6)	249		atomic (1-230)	6ZOJ	Docked & adjusted	Core map
	L7	L7	S7/S7 (eS7)	194		atomic (8-100, 119-193)	6ZOJ	Docked & adjusted	Core map
	L8	L8	S8/S8 (eS8)	208		atomic (2-125, 151-206)	6ZOJ	Docked & adjusted	Core map
	L9	L9	S9/S9 (uS4)	194		atomic (2-181)	6ZOJ	Docked & adjusted	Core map
	LC	LC	S16/S16 (uS9)	146		atomic (5-140)	6ZOJ	Docked & adjusted	Core map
	LD	LD	S11/S11 (uS17)	158		atomic (2-152)	6ZOJ	Docked & adjusted	Core map
	LF	LF	S24/S24 (eS24)	133		atomic (1-126)	6ZOJ	Docked & adjusted	Core map
	LG	LG	S28/S28 (eS28)	69		atomic (7-68)	6ZOJ	Docked & adjusted	Core map
	SR	SR	S23/S23 (uS12)	143		atomic (2-142)	6ZOJ	Docked & adjusted	Core map
	NF	NF	S13/S13 (uS15)	151		atomic (2-150)	6ZOJ	Docked & adjusted	Core map
	NG	NG	S14/S14 (uS11)	151		atomic (25-151)	6ZOJ	Docked & adjusted	Core map
	NM	NM	S3A/S1 (eS1)	264		atomic (10-233)	6ZOJ	Docked & adjusted	Core map
	NO	NO	S15A/S22 (uS8)	130		atomic (2-130)	6ZOJ	Docked & adjusted	Core map
	NP	NP	S19/S19 (eS19)	145		atomic (2-145)	6ZOJ	Docked & adjusted	S19 map
	NQ	NQ	S27/S27 (eS27)	84		atomic (2-83, Zn^{2+})	6ZOJ	Docked & adjusted	Core map
	NT	NT	S27A/S31 (eS31)	156		atomic (92-149, Zn^{2+})	6ZOJ	Docked & adjusted	Core map
	LA	LA	S12/S12 (eS12)	132		atomic (11-130)	5AJ0	Docked & adjusted	Core map
	NU	NU	S17/S17 (eS17)	135		atomic (5-64)	6ZOJ	Docked & adjusted	Core map
UTP-A	LH	LH	WDR75/Utp17	830	Tandem WDR40 CTD	atomic (7-671) atomic (692-703, 716-759, 803-827)	5WLC/6ZQD	Deeptracer, homology model & manual building	UTP-A map
	LI	LI	NOL11/Utp8	719	WDR40 CTD	atomic (152-161, 165-183, 189-195, 205-234, 242-255, 262-277) atomic (286-303, 310-322), poly-A (8-48, 59-92, 104-147, 325-346) atomic (354-360, 396-515, 577-718)	5WLC/6ZQD	Deeptracer, homology model & manual building	NOL11 map
	LJ	LJ	UTP15/Utp15	518	WDR40 CTD	atomic (2-13, 21-318) atomic (343-494)	5WLC/6ZQD	Deeptracer, homology model & manual building	UTP-A map
	LK	LK	WDR43/Utp5	677	CTD	atomic (463-580)	5WLC/6ZQD	Homology model & manual building	UTP-A map
	LL	LL	WDR43/Utp5	677	WDR40 Linker CTD	atomic (9-69, 93-322, 331-375) atomic (376-413) atomic (456-580, 594-604)	5WLC/6ZQD	Deeptracer & manual building	UTP-A map
	LN	LN	UTP4/Utp4	686	Tandem WDR40	atomic (2-623, 638-686)	5WLC/6ZQD	Homology model & manual building	UTP-A map
	LM	LM	HEATR1/Utp10	2144	HEAT repeat	atomic (2-1166, 1202-1361, 1368-1428, 1438-1476, 1495-1653) atomic (1662-1877, 1889-1924, 1932-2007, 2013-2055, 2059-2144)	5WLC/6ZQD	Deeptracer, homology model & manual building	HEATR1 map
UTP-B	LO	LO	PWP2/Utp1	919	Tandem WDR40 CTD	atomic (2-227, 271-588, 606-731) atomic (732-880)	5WLC/6ZQD	Homology model & manual building	Core map
	LP	LP	UTP6/Utp6	597	Helical repeat	atomic (1-200, 213-283, 297-339, 346-597)	5WLC/6ZQD	Homology model & manual building	UTP6 map
	LQ	LQ	WDR3/Utp12	943	Tandem WDR40 CTD	atomic (5-223, 261-332, 341-373, 377-395, 403-526, 537-721) atomic (753-782, 793-940)	5WLC/6ZQD	Deeptracer, homology model & manual building	Core map
	LR	LR	TBL3/Utp13	808	Tandem WDR40 CTD	atomic (11-457, 464-635) atomic (636-788)	5WLC/6ZQD	Homology model & manual building	UTP-C map
	LS	LS	UTP18/Utp18	556	NTD WDR40	atoms (62-111, 138-198) atoms (215-556)	5WLC/6ZQD	Homology model & manual building	Core map
	LT	LT	WDR36/Utp21	951	Tandem WDR40 Linker CTD	atomic (64-425, 439-490, 495-721) atomic (735-759) atomic (760-948)	5WLC/6ZQD	Homology model & manual building	Core map
U3 snoRNP	SA	SA	NOP56/Nop56	594	NTD CTD	atomic (2-86, 90-161) atomic (162-340, 353-412)	5WLC/6ZQD	Deeptracer, homology model & manual building	Core map
	SB	SB	NOP58/Nop58	529	NTD CTD CTD extension	atomic (1-154) atomic (155-409) atomic (418-438)	5WLC/6ZQD	Deeptracer, homology model & manual building	Core map
	SC	SC	FBRL/Nop1	321		atomic (85-126, 132-318)	2IPX	Docked & adjusted	Core map
	SD	SD	FBRL/Nop1	321		atomic (78-126, 132-318)	2IPX	Docked & adjusted	Core map
	SE	SE	hSNU13/Snu13	128		atomic (6-128)	2OZB	Docked & adjusted	Core map
	SF	SF	hSNU13/Snu13	128		atomic (4-128)	2OZB	Docked & adjusted	Core map
	SG	SG	U3IP2/Rrp9	475	NTD WDR40	atomic (73-99, 103-125) atomic (126-189, 194-468)	4JXM	Homology model & manual building Docked & adjusted	Core & UTP20 map

Subcomplex	Chain ID	SegID	Molecule name (human/yeast)	Total residues or bases	Domains	Modelled (residues range)	Modeling template	Modeling method	Maps used for building
Other ribosome assembly factors	LU	LU	DCA13/Sof1	445	NTD WDR40 CTD	atomic (1-55) atomic (56-355) atomic (356-445)	5WLC/6ZQD	Homology model & manual building	Core map
	LW	LW	WDR46/Utp7	610	NTD WDR40 CTD	atomic (142-186) atomic (187-475) atomic (476-588)	5WLC/6ZQD	Homology model & manual building	Core map
	LZ	LZ	IMP3/Imp3	184		atomic (2-22, 42-182)	5WLC/6ZQD	Homology model & manual building	Core map
	SH	SH	RCL1/Rcl1	373		atomic (6-373)	5WLC/6ZQD	Homology model & manual building	Core map
	SI	SI	BMS1/Bms1	1282	GTPase RCL1 interaction CTD	atomic (5-27, 33-344, 844-1131, GTP, Mg^{2+}) atomic (681-695, 727-760) atomic (1132-1262)	5WLC/6ZQD	Deeptracer, homology model & manual building	Core map
	SJ	SJ	NEP1/Emg1	244		atomic (41-244, SAH)	5FAI	Docked & adjusted	NOC4-NOP14 map
	SK	SK	NEP1/Emg1	244		atomic (41-244, SAH)	5FAI	Docked & adjusted	NOC4-NOP14 map
	SL	SL	FCF1/Utp24	198		atomic (2-16, 39-198, Zn^{2+}, Mg^{2+})	5WLC/6ZQD	Homology model & manual building	Core map
	SM	SM	IMP4/Imp4	291		atomic (1-51, 72-290)	5WLC/6ZQD	Homology model & manual building	Core map
	SW	SW	PNO1/Pno1	252		atomic (58-252)	6G18	Docked & adjusted	Core map
	SP	SP	UTP20/Utp20	2785	Helical repeat	atomic (11-474, 492-662, 672-776, 787-871, 906-1282, 1292-1313) atomic (1325-1435, 1446-1690, 1772-2503, 2513-2570, 2618-2723)		Deeptracer & manual building	UTP20 map
	SQ	SQ	TDIF2/Fcf2	756		atomic (560-582, 593-611, 631-744)	5WLC/6ZQD	Homology model & manual building	Core map
	SS	SS	UTP14/Utp14	771		atomic (63-162, 170-194, 205-246, 550-586, 590-735)		Deeptracer & manual building	Core map
	ST	ST	NOP14/Nop14	857	NTD Helical repeat CTD	atomic (29-86, 274-298), poly-A (186-234, 246-273) atomic (463-488, 493-665, 679-745), poly-A (414-462) atomic (746-772, 787-854)	5WLC/6ZQD	Deeptracer, homology model & manual building	Core & NOC4-NOP14 map
	SU	SU	NOC4L/Noc4L	516	Helical repeat	poly-A (7-25, 27-45, 48-68, 78-124, 158-169), atomic (141-153, 177-513)	5WLC/6ZQD	Homology model & manual building	NOC4-NOP14 map
	SY	SY	UTP11/Utp11	253		atomic (1-72, 89-253)	5WLC/6ZQD	Homology model & manual building	Core map
	SZ	SZ	BYST/Enp1	437	Helical repeat	poly-A (130-164, 169-178), atomic (179-423)	6G18	Docked, adjusted & manual building	BYST map
	NA	NA	MPP10/Mpp10	681		atomic (355-447, 457-600, 611-660, 674-681)		Deeptracer & manual building	Core map
	NB	NB	SAS10/Sas10	479		atomic (34-63, 407-479)	5WLC/6ZQD	Homology model & manual building	Core map
	NH	NH	NOL6/Utp22	1146		atomic (76-1141, ATP, Mg^{2+})	5WLC/6ZQD	Deeptracer, homology model & manual building	NOL6-RRP7 map
	NI	NI	RRP7A/Rrp7	280		atomic (18-251)	5WLC/6ZQD	Homology model & manual building	NOL6-RRP7 map
	ND	ND	NOL7/Bud21	257		atomic (168-250)		Deeptracer & manual building	Core map
	NR	NR	RRP12/Rrp12	1297	Helical repeat	poly-A (74-1029)	6G4S	Docked & adjusted	RRP12 map
Post-A1 specific assembly factors	NS	NS	DHX37/Dhr1	1157	NTD Helicase CTD	atomic (3-14, 27-57, 78-152) side chains trimmed (235-435, 450-493, 586-610, 612-748, 763-818, 823-905, 911-936) atomic (1016-1157) / trimmed side chains (937-1015)	yeast Dhr1 core (this study) 6O16	Deeptracer, homology model & manual building	Core & DHX37 map
	NL	NL	DIM1/Dim1	313		atomic (36-313)	6W6C	Docked & adjusted	Core map
	LY	LY	AROS/?	136		atomic (2-17, 45-107, 120-135)		Manual building	Core & HEATR1 map
Exosome	NV	NV	EXOSC10/Rrp6	885		atomic (815-830, 837-844, 861-871, 879-884)		Manual building	UTP20 map
	SX	SX	Unassigned peptide	228		poly-A (5 segments)		Manual building	Core & HEATR1-UNK map

Table S2. Summary of model building for the human SSU processome in state post-A1.

Subcomplex	Chain ID	SegID	Molecule name (human/yeast)	Total residues or bases	Domains	Modelled (residues range)	Modeling template	Modeling method	Maps used for building
RNA	L0	L0	5'ETS rRNA	3620		atomic (431-470,597-617,657-695,709-763,795-806,811-844,850-866,1412-1435)		Manual building	UTP-A & 5'ETS maps
	N0	N0	5'ETS rRNA	3620		abasic (871-881, 1396-1416)		Manual building	UTP-A & 5'ETS maps
	L1	L1	pre-18S rRNA	1880		atomic (2-40,45-50,55-135,140-196,203-240,246-251,268-289,295-408,411-471,476-628,635-655,672-687,916-1035,1090-1148,1169-1179,1186-1237,1265-1323,1345-1359,1364-1400,1446-1503,1510-1516,1523-1551,1588-1599,1637-1692,1695-1826,1837-1860 + 19 Mg^{2+})	Post-A1 state	Docked & rebuilt	Core & UTP-C maps
	L2	L2	U3 snoRNA	217		atomic (3-217)		Manual building	Core map
Ribosomal proteins	L3	L3	S18/S18 (uS13)	152		atomic (3-87), poly-A (88-116) / *trimmed side chains in pre-A1**	Post-A1 state	Docked & adjusted	Core map
	L4	L4	S4X/S4 (eS4)	263		atomic (2-263)[1]	Post-A1 state	Docked & adjusted	Core map
	L5	L5	S5/S5 (uS7)	204		atomic (15-204)	Post-A1 state	Docked & adjusted	Core map
	L6	L6	S6/S6 (eS6)	249		atomic (1-78, 91-230)	Post-A1 state	Docked & adjusted	Core map
	L7	L7	S7/S7 (eS7)	194		atomic (8-100, 119-193)	Post-A1 state	Docked & adjusted	Core map
	L8	L8	S8/S8 (eS8)	208		atomic (2-125, 151-206)	Post-A1 state	Docked & adjusted	Core map
	L9	L9	S9/S9 (uS4)	194		atomic (11-181)	Post-A1 state	Docked & adjusted	Core map
	LC	LC	S16/S16 (uS9)	146		atomic (5-143)	Post-A1 state	Docked & adjusted	Core map
	LD	LD	S11/S11 (uS17)	158		atomic (2-148)	Post-A1 state	Docked & adjusted	Core map
	LF	LF	S24/S24 (eS24)	133		atomic (1-104)	Post-A1 state	Docked & adjusted	Core map
	LG	LG	S28/S28 (eS28)	69		atomic (7-68)	Post-A1 state	Docked & adjusted	Core map
	SR	SR	S23/S23 (uS12)	143		atomic (35-142)	Post-A1 state	Docked & adjusted	Core map
	NF	NF	S13/S13 (uS15)	151		atomic (2-150)	Post-A1 state	Docked & adjusted	Core map
	NG	NG	S14/S14 (uS11)	151		atomic (25-140)	Post-A1 state	Docked & adjusted	Core map
	NM	NM	S3A/S1 (eS1)	264		atomic (10-233, 245-253)	Post-A1 state	Docked & adjusted	Core map
	NO	NO	S15A/S22 (uS8)	130		atomic (2-130)	Post-A1 state	Docked & adjusted	Core map
	NQ	NQ	S27/S27 (eS27)	84		atomic (2-83, Zn^{2+})	Post-A1 state	Docked & adjusted	Core map
	NT	NT	S27A/S31 (eS31)	156		atomic (92-149, Zn^{2+}) / *trimmed side chains in pre-A1**	Post-A1 state	Docked & adjusted	Core map
	LA	LA	S12/S12 (eS12)	132		atomic (11-130) / *trimmed side chains in pre-A1**	Post-A1 state	Docked & adjusted	Core map
	NU	NU	S17/S17 (eS17)	135		atomic (5-64) / *trimmed side chains in pre-A1**	Post-A1 state	Docked & adjusted	Core map
UTP-A	LH	LH	WDR75/Utp17	830	Tandem WDR40 CTD	atomic (7-671) atomic (692-703, 716-759, 803-827)	Post-A1 state	Docked & adjusted	UTP-A map
	LI	LI	NOL11/Utp8	719	WDR40 CTD	atomic (152-161, 165-183, 189-195, 205-234, 242-255, 262-277) *trimmed side chains in pre-A1** atomic (286-303, 310-322), poly-A (8-48, 59-92, 104-147, 325-346) atomic (354-360, 396-515, 577-718)	Post-A1 state	Docked & adjusted	UTP-A map
	LJ	LJ	UTP15/Utp15	518	WDR40 CTD	atomic (2-318) atomic (343-494)	Post-A1 state	Docked, adjusted & manual building	UTP-A map
	LK	LK	WDR43/Utp5	677	CTD	atomic (463-580)	Post-A1 state	Docked & adjusted	UTP-A map
	LL	LL	WDR43/Utp5	677	WDR40 Linker CTD	atomic (9-69, 93-322, 331-375) atomic (376-413) atomic (456-580, 594-604)	Post-A1 state	Docked & adjusted	UTP-A map
	LN	LN	UTP4/Utp4	686	Tandem WDR40	atomic (2-623, 638-686)	Post-A1 state	Docked & adjusted	UTP-A map
	LM	LM	HEATR1/Utp10	2144	HEAT repeat	atomic (2-1166, 1202-1361, 1368-1428, 1438-1454, 1457-1472, 1507-1537, 1545-1595, 1598-1653, 1662-1876, 1889-1924, 1932-1970, 1979-2007, 2013-2055, 2059-2144) *trimmed side chains in pre-A1* (2-1119)*	Post-A1 state	Docked & adjusted	HEATR1 map
UTP-B	LO	LO	PWP2/Utp1	919	Tandem WDR40 CTD	atomic (2-239, 269-731) atomic (732-880)	Post-A1 state	Docked, adjusted & manual building	Core map
	LP	LP	UTP6/Utp6	597	Helical repeat	atomic (1-200, 213-283, 297-339, 346-597)	Post-A1 state	Docked & adjusted	Core map
	LQ	LQ	WDR3/Utp12	943	Tandem WDR40 CTD	atomic (5-223, 261-332, 341-373, 377-395, 403-526, 537-721) atomic (753-782, 793-917, 923-943)	Post-A1 state	Docked & adjusted	Core map
	LR	LR	TBL3/Utp13	808	Tandem WDR40 CTD	atomic (11-457, 464-635) / *trimmed side chains in pre-A1** atomic (636-788)	Post-A1 state	Docked & adjusted	TBL3 map
	LS	LS	UTP18/Utp18	556	NTD WDR40	atoms (57-112, 138-198) atoms (215-556)	Post-A1 state	Docked & adjusted	Core map
	LT	LT	WDR36/Utp21	951	Tandem WDR40 Linker CTD	atomic (64-721) atomic (735-759) atomic (760-806, 810-948)	Post-A1 state	Docked & adjusted	Core map
U3 snoRNP	SA	SA	NOP56/Nop56	594	NTD CTD	atomic (2-86, 90-161) atomic (162-340, 353-412)	Post-A1 state	Docked & adjusted	Core map
	SB	SB	NOP58/Nop58	529	NTD CTD	atomic (1-154) atomic (155-400)	Post-A1 state	Docked & adjusted	Core map
	SC	SC	FBRL/Nop1	321		atomic (85-126, 131-317)	Post-A1 state	Docked & adjusted	Core map
	SD	SD	FBRL/Nop1	321		atomic (78-126, 131-318)	Post-A1 state	Docked & adjusted	Core map
	SE	SE	SNU13/Snu13	128		atomic (6-128)	Post-A1 state	Docked & adjusted	Core map
	SF	SF	SNU13/Snu13	128		atomic (4-128)	Post-A1 state	Docked & adjusted	Core map
	SG	SG	U3IP2/Rrp9	475	NTD WDR40	atomic (73-99, 103-125) / *trimmed side chains* atomic (126-189, 194-468)	Post-A1 state	Docked & adjusted	Core & NGDN maps

Subcomplex	Chain ID	SegID	Molecule name (human/yeast)	Total residues or bases	Domains	Modelled (residues range)	Modeling template	Modeling method	Maps used for building
Other ribosome assembly factors	LU	LU	DCA13/Sof1	445	NTD WDR40 CTD	atomic (1-55) atomic (56-355) atomic (356-445)	Post-A1 state		Core map
	LW	LW	WDR46/Utp7	610	NTD WDR40 CTD	atomic (95-186) atomic (187-475) atomic (476-588)	Post-A1 state	Docked, adjusted & manual building	Core map
	LZ	LZ	IMP3/Imp3	184		atomic (2-184)	Post-A1 state	Docked, adjusted & manual building	Core map
	SH	SH	RCL1/Rcl1	373		atomic (6-373)	Post-A1 state	Docked & adjusted	Core map
	SI	SI	BMS1/Bms1	1282	GTPase RCL1 interaction NAT10 interaction CTD	atomic (49-355, 844-1131, GTP, Mg^{2+}) atomic (687-695, 727-760) atomic (369-402, 664-681), poly-A (625-631) atomic (1132-1276)	Post-A1 state	Docked, adjusted & manual building	Core map
	SJ	SJ	NEP1/Emg1	244		atomic (41-244, SAH) / *trimmed side chains in pre-A1**	Post-A1 state	Docked & adjusted	NEP1 map
	SK	SK	NEP1/Emg1	244		atomic (41-244, SAH)	Post-A1 state	Docked & adjusted	NEP1 map
	SL	SL	UTP24/Utp24	198		atomic (7-198, Zn^{2+}, Mg^{2+})	Post-A1 state	Docked, adjusted & manual building	Core map
	SM	SM	IMP4/Imp4	291		atomic (1-290)	Post-A1 state	Docked, adjusted & manual building	Core map
	SW	SW	PNO1/Pno1	252		atomic (58-252) / *trimmed side chains in pre-A1**	Post-A1 state	Docked & adjusted	PNO1 map
	SP	SP	UTP20/Utp20	2785	Helical repeat	atomic (2-474, 492-662, 672-776, 787-871, 906-1282, 1292-1313, 1325-1435) atomic (1446-1690, 1772-1797, 1815-1938, 1958-2032, 2050-2066, 2077-2238) *trimmed side chains in pre-A1* (201-642, 1048-2238)*	Post-A1 state	Docked & adjusted	UTP20-Nterm & UTP20-Cterm maps
	SQ	SQ	TDIF2/Fcf2	756		atomic (548-582, 593-744)	Post-A1 state	Docked, adjusted & manual building	Core map
	SS	SS	UTP14A/Utp14	771		atomic (121-209, 217-250, 663-737)	Post-A1 state	Docked, adjusted & manual building	Core map
	ST	ST	NOP14/Nop14	857	NTD Helical repeat CTD	atomic (29-86, 274-298), poly-A (186-234, 246-273) / *trimmed side chains in pre-A1** atomic (463-488, 493-665, 679-745), poly-A (414-462) / *trimmed side chains in pre-A1** atomic (746-772, 787-854)	Post-A1 state	Docked, adjusted & manual building	Core & NOC4-NOP14 maps
	SU	SU	NOC4L/Noc4L	516	Helical repeat	poly-A (7-25, 27-45, 48-68, 78-124, 158-169), atomic (141-153, 177-513) *trimmed side chains in pre-A1**	Post-A1 state	Docked & adjusted	NOC4-NOP14 map
	SY	SY	UTP11/Utp11	253		atomic (1-126, 133-175, 185-253)	Post-A1 state	Docked, adjusted & manual building	Core map
	SZ	SZ	BYST/Enp1	437	Helical repeat	poly-A (130-164, 169-178), atomic (179-423) / *trimmed side chains in pre-A1**	Post-A1 state	Docked	BYST map
	NA	NA	MPP10/Mpp10	681		atomic (355-463, 468-599, 674-681)	Post-A1 state	Docked, adjusted & manual building	Core map
	NB	NB	SAS10/Sas10	479		atomic (407-479)	Post-A1 state	Docked & adjusted	Core map
	NH	NH	NOL6/Utp22	1146		atomic (76-1141, ATP, Mg^{2+}) / *trimmed side chains in pre-A1**	Post-A1 state	Docked & adjusted	NOL6-RRP7 map
	NI	NI	RRP7A/Rrp7	280		atomic (18-251) / trimmed side chains in pre-A1* (18-164)	Post-A1 state	Docked & adjusted	NOL6-RRP7 map
	ND	ND	NOL7/Bud21	257		atomic (169-252)		Deeptracer & manual building	Core map
	NR	NR	RRP12/Rrp12	1297	Helical repeat	poly-A (74-1029)	Post-A1 state	Docked	RRP12 map
Pre-A1 specific assembly factors	NY	NY	KRR1/Krr1	381	KH domain CTD	atomic (39-246) atomic (264-329)	5WLC	Homology model & manual building	Core map
	NJ	NJ	NAT10/Kre33	1025	NTD Helicase N-acetyltransferase CTD	atomic (1-77, 89-174, 178-221) atomic (228-414, 423-434, 457-470) atomic (471-585, 602-658, 669-751) atomic (762-913)		Deeptracer, de novo homology model (TrRosetta) & manual building	NAT10-NOL10 map
	NK	NK	NAT10/Kre33	1025	NTD Helicase N-acetyltransferase CTD	atomic (1-61, 91-221) / trimmed side chains in pre-A1* atomic (231-434, 457-470, ATP) / trimmed side chains in pre-A1* atomic (471-596, 602-657, 689-752) / trimmed side chains in pre-A1* atomic (762-913) / trimmed side chains in pre-A1*		Deeptracer, de novo homology model (TrRosetta) & manual building	NAT10-NOL10 map
	NW	NW	NOL10/Enp2	688	WDR40	atomic (7-14, 43-216, 230-358)		Deeptracer, de novo homology model (TrRosetta) & manual building	NAT10-NOL10 map
	NN	NN	AATF	560		atomic (509-550)		Manual building	NAT10-NOL10 map
	NC	NC	NGDN/Lep5††	315		atomic (189-282)		Manual building	NGDN map
	NE	NE	C1ORF131/Faf1	293		atomic (166-236, 253-261, 269-288)		BackPhyre using Faf1 sequence & Manual building	Core map
	SX	SX	Unassigned peptide			poly-A (2 segments)	Post-A1 state	Docked	Core & HEATR1 map

† Fragment 241-263 not visible in state pre-A1*.
†† NGDN not present in state pre-A1*.

Table S3. Summary of model building for the human SSU processome in state pre-A1 and pre-A1*.

Data collection and Processing			
Microscope		FEI Titan Krios	
Voltage (keV)		300	
Camera		Gatan K3	
Magnification		64,000	
Pixel size at detector (Å/pixel)		1.08	
Total electron exposure ($e^-/Å^2$)		58	
Exposure rate (e^-/pixel/sec)		30.1	
Number of frames collected (no.)		45	
Defocus range (μm)		0.7 - 2.7	
Automation software		SerialEM	
Micrographs collected (no.)		84,904	
Total extracted particles (no.)		9,297,626	
	pre-A1	**pre-A1***	**post-A1**
EMDB	EMD-23936	EMD-23937	EMD-23938
PDB	7MQ8	7MQ9	7MQA
Final particle images (no.)	42,142	21,096	459,775
Point-group symmetry	C1	C1	C1
Resolution (global at FSC 0.143, Å)			
Raw map	3.51	3.87	2.65
Composite map	3.60	N/A	2.69
Resolution range (local at FSC0.5, Å)			
Raw map	3.3-10.9	3.5-11.7	2.4-8.9
Composite map	3.4-11.4	N/A	2.5-10.4
Map sharpening *B* factor ($Å^2$)	-44.44	-57.59	-47.02
Model refinement			
Refinement package (real space)	phenix.real_space_refine (1.19)		
Initial models used (PDB code)	6ZOJ/5AJ0/5WLC/6ZQD/2IPX/2OZB/4JXM/5FAI/6G18/6W6C/6G4S		
Model resolution cutoff (Å)	3.8	4.0	2.8
Model composition			
Non-hydrogen atoms	245,114	223,186	242,409
Protein residues	26,636	26,490	26,363
RNA	1780	1780	1828
Ligands	GTP 1x, ATP 2x, Zn^{2+} 3x, Mg^{2+} 22x	GTP 1x, ATP 2x, Zn^{2+} 3x, Mg^{2+} 22x	GTP 1x, ATP 1x, Zn^{2+} 3x, Mg^{2+} 64x
B-factors			
B-factors (A^2)			
Protein	92.27	68.95	65.98
RNA	159.83	143.02	93.71
Ligand	80.37	98.82	62.19
RMSDs			
Bond lengths (Å)	0.004	0.004	0.004
Bond angles (°)	0.925	0.918	0.920
Validation			
MolProbity score	1.31	1.28	1.29
CaBLAM outliers	1.41	1.44	1.31
Clash score	5.73	5.15	5.16
Poor rotamers (%)	0.02	0.04	0.04
C-beta deviations	0	0	0
EMRinger score	1.78	1.95	2.69
Ramachandran plot			
Favored (%)	98.08	97.99	97.93
Allowed (%)	1.92	2.01	2.07
Outliers (%)	0	0	0
RNA validation			
Average suiteness (%)	47.8	47.6	49.3
Good sugar puckers (%)	98.15	98.26	98.64

Table S4. Cryo-EM data collection and refinement statistics.

	Dhr1 core
PDB entry	7MQJ
Crystal form	$P2_1$
Unit cell dimensions	
a, *b*, *c* (Å)	41.77, 130.94, 86.08
α, β, γ (°)	90.00, 106.483, 90.00
Data collection	
Wavelength (Å)	0.97919
Resolution (Å)	38.58-2.23 (2.31-2.23)*
Unique reflections	42918 (4275)
R_{meas} (%)	9.7 (61.9)
$CC_{1/2}$	99.7 (78.4)
Completeness (%)	99.34 (98.68)
$I / \sigma I$	11.89 (2.11)
Multiplicity	3.4 (3.3)
Model statistics	
Model composition	
No. atoms	
Protein	6303
Ligand/ion	28
Water	284
Refinement	
Resolution (Å)	38.58-2.23
No. reflections	42910
R_{work} / R_{free}	0.1794/0.2275
B-factors	
Protein	51.2
Ligand/ion	50.1
Water	43.5
R.m.s. deviations:	
Bond lengths (Å)	0.0082
Bond angles (°)	0.96
Ramachandran plot:	
favored (%)	96.35
allowed (%)	3.52
outliers (%)	0.28
Clashscore	6
Number of TLS group	5

*Values in parentheses are for highest-resolution shell.

Table S5. X-ray data collection and refinement statistics.

References and Notes

1. K. E. Bohnsack, M. T. Bohnsack, Uncovering the assembly pathway of human ribosomes and its emerging links to disease. *EMBO J.* **38**, e100278 (2019). doi:10.15252/embj.2018100278 Medline

2. D. L. J. Lafontaine, J. A. Riback, R. Bascetin, C. P. Brangwynne, The nucleolus as a multiphase liquid condensate. *Nat. Rev. Mol. Cell Biol.* **22**, 165–182 (2021). doi:10.1038/s41580-020-0272-6 Medline

3. B. Michot, J. P. Bachellerie, Secondary structure of the 5′ external transcribed spacer of vertebrate pre-rRNA. Presence of phylogenetically conserved features. *Eur. J. Biochem.* **195**, 601–609 (1991). doi:10.1111/j.1432-1033.1991.tb15743.x Medline

4. M. Hunziker, J. Barandun, O. Buzovetsky, C. Steckler, H. Molina, S. Klinge, Conformational switches control early maturation of the eukaryotic small ribosomal subunit. *eLife* **8**, e45185 (2019). doi:10.7554/eLife.45185 Medline

5. R.-W. Yao, G. Xu, Y. Wang, L. Shan, P.-F. Luan, Y. Wang, M. Wu, L.-Z. Yang, Y.-H. Xing, L. Yang, L.-L. Chen, Nascent pre-rRNA sorting via phase separation drives the assembly of dense fibrillar components in the human nucleolus. *Mol. Cell* **76**, 767–783.e11 (2019). doi:10.1016/j.molcel.2019.08.014 Medline

6. F. Dragon, J. E. G. Gallagher, P. A. Compagnone-Post, B. M. Mitchell, K. A. Porwancher, K. A. Wehner, S. Wormsley, R. E. Settlage, J. Shabanowitz, Y. Osheim, A. L. Beyer, D. F. Hunt, S. J. Baserga, A large nucleolar U3 ribonucleoprotein required for 18S ribosomal RNA biogenesis. *Nature* **417**, 967–970 (2002). doi:10.1038/nature00769 Medline

7. M. Chaker-Margot, M. Hunziker, J. Barandun, B. D. Dill, S. Klinge, Stage-specific assembly events of the 6-MDa small-subunit processome initiate eukaryotic ribosome biogenesis. *Nat. Struct. Mol. Biol.* **22**, 920–923 (2015). doi:10.1038/nsmb.3111 Medline

8. L. Zhang, C. Wu, G. Cai, S. Chen, K. Ye, Stepwise and dynamic assembly of the earliest precursors of small ribosomal subunits in yeast. *Genes Dev.* **30**, 718–732 (2016). doi:10.1101/gad.274688.115 Medline

9. M. Kornprobst, M. Turk, N. Kellner, J. Cheng, D. Flemming, I. Koš-Braun, M. Koš, M. Thoms, O. Berninghausen, R. Beckmann, E. Hurt, Architecture of the 90S pre-ribosome: A structural view on the birth of the eukaryotic ribosome. *Cell* **166**, 380–393 (2016). doi:10.1016/j.cell.2016.06.014 Medline

10. M. Chaker-Margot, J. Barandun, M. Hunziker, S. Klinge, Architecture of the yeast small subunit processome. *Science* **355**, eaal1880 (2017). doi:10.1126/science.aal1880 Medline

11. J. Barandun, M. Chaker-Margot, M. Hunziker, K. R. Molloy, B. T. Chait, S. Klinge, The complete structure of the small-subunit processome. *Nat. Struct. Mol. Biol.* **24**, 944–953 (2017). doi:10.1038/nsmb.3472 Medline

12. J. Cheng, N. Kellner, O. Berninghausen, E. Hurt, R. Beckmann, 3.2-Å-resolution structure of the 90S preribosome before A1 pre-rRNA cleavage. *Nat. Struct. Mol. Biol.* **24**, 954–964 (2017). doi:10.1038/nsmb.3476 Medline

13. J. Cheng, B. Lau, G. La Venuta, M. Ameismeier, O. Berninghausen, E. Hurt, R. Beckmann, 90*S* pre-ribosome transformation into the primordial 40*S* subunit. *Science* **369**, 1470–1476 (2020). doi:10.1126/science.abb4119 Medline

14. Y. Du, W. An, X. Zhu, Q. Sun, J. Qi, K. Ye, Cryo-EM structure of 90*S* small ribosomal subunit precursors in transition states. *Science* **369**, 1477–1481 (2020). doi:10.1126/science.aba9690 Medline

15. B. Lau, J. Cheng, D. Flemming, G. La Venuta, O. Berninghausen, R. Beckmann, E. Hurt, Structure of the maturing 90S pre-ribosome in association with the RNA exosome. *Mol. Cell* **81**, 293–303.e4 (2021). doi:10.1016/j.molcel.2020.11.009 Medline

16. M. Ameismeier, J. Cheng, O. Berninghausen, R. Beckmann, Visualizing late states of human 40S ribosomal subunit maturation. *Nature* **558**, 249–253 (2018). doi:10.1038/s41586-018-0193-0 Medline

17. M. Ameismeier, I. Zemp, J. van den Heuvel, M. Thoms, O. Berninghausen, U. Kutay, R. Beckmann, Structural basis for the final steps of human 40S ribosome maturation. *Nature* **587**, 683–687 (2020). doi:10.1038/s41586-020-2929-x Medline

<jrn>18. L. Tafforeau, C. Zorbas, J.-L. Langhendries, S.-T. Mullineux, V. Stamatopoulou, R. Mullier, L. Wacheul, D. L. J. Lafontaine, The complexity of human ribosome biogenesis revealed by systematic nucleolar screening of Pre-rRNA processing factors. *Mol. Cell* **51**, 539–551 (2013). doi:10.1016/j.molcel.2013.08.011 Medline</jrn>

19. L. Badertscher, T. Wild, C. Montellese, L. T. Alexander, L. Bammert, M. Sarazova, M. Stebler, G. Csucs, T. U. Mayer, N. Zamboni, I. Zemp, P. Horvath, U. Kutay, Genome-wide RNAi screening identifies protein modules required for 40S subunit synthesis in human cells. *Cell Rep.* **13**, 2879–2891 (2015). doi:10.1016/j.celrep.2015.11.061 Medline

20. K. I. Farley-Barnes, K. L. McCann, L. M. Ogawa, J. Merkel, Y. V. Surovtseva, S. J. Baserga, Diverse regulators of human ribosome biogenesis discovered by changes in nucleolar number. *Cell Rep.* **22**, 1923–1934 (2018). doi:10.1016/j.celrep.2018.01.056 Medline

21. S. B. Sondalle, S. J. Baserga, Human diseases of the SSU processome. *Biochim. Biophys. Acta* **1842**, 758–764 (2014). doi:10.1016/j.bbadis.2013.11.004 Medline

22. S. K. Natchiar, A. G. Myasnikov, H. Kratzat, I. Hazemann, B. P. Klaholz, Visualization of chemical modifications in the human 80S ribosome structure. *Nature* **551**, 472–477 (2017). doi:10.1038/nature24482 Medline

23. M. Taoka, Y. Nobe, Y. Yamaki, K. Sato, H. Ishikawa, K. Izumikawa, Y. Yamauchi, K. Hirota, H. Nakayama, N. Takahashi, T. Isobe, Landscape of the complete RNA chemical modifications in the human 80S ribosome. *Nucleic Acids Res.* **46**, 9289–9298 (2018). doi:10.1093/nar/gky811 Medline

24. J. Cheng, J. Baßler, P. Fischer, B. Lau, N. Kellner, R. Kunze, S. Griesel, M. Kallas, O. Berninghausen, D. Strauss, R. Beckmann, E. Hurt, Thermophile 90S pre-ribosome structures reveal the reverse order of co-transcriptional 18S rRNA subdomain integration. *Mol. Cell* **75**, 1256–1269.e7 (2019). doi:10.1016/j.molcel.2019.06.032 Medline

25. S. Kass, N. Craig, B. Sollner-Webb, Primary processing of mammalian rRNA involves two adjacent cleavages and is not species specific. *Mol. Cell. Biol.* **7**, 2891–2898 (1987). doi:10.1128/MCB.7.8.2891 Medline

26. N. J. Watkins, M. T. Bohnsack, The box C/D and H/ACA snoRNPs: Key players in the modification, processing and the dynamic folding of ribosomal RNA. *WIREs RNA* **3**, 397–414 (2012). doi:10.1002/wrna.117 Medline

27. Q. Sun, X. Zhu, J. Qi, W. An, P. Lan, D. Tan, R. Chen, B. Wang, S. Zheng, C. Zhang, X. Chen, W. Zhang, J. Chen, M.-Q. Dong, K. Ye, Molecular architecture of the 90S small subunit pre-ribosome. *eLife* **6**, e22086 (2017). doi:10.7554/eLife.22086 Medline

28. E. V. Wasmuth, C. D. Lima, The Rrp6 C-terminal domain binds RNA and activates the nuclear RNA exosome. *Nucleic Acids Res.* **45**, 846–860 (2017). doi:10.1093/nar/gkw1152 Medline

29. M. Thoms, E. Thomson, J. Baßler, M. Gnädig, S. Griesel, E. Hurt, The exosome is recruited to RNA substrates through specific adaptor proteins. *Cell* **162**, 1029–1038 (2015). doi:10.1016/j.cell.2015.07.060 Medline

30. F. M. Boneberg, T. Brandmann, L. Kobel, J. van den Heuvel, K. Bargsten, L. Bammert, U. Kutay, M. Jinek, Molecular mechanism of the RNA helicase DHX37 and its activation by UTP14A in ribosome biogenesis. *RNA* **25**, 685–701 (2019). doi:10.1261/rna.069609.118 Medline

31. A. Roychowdhury, C. Joret, G. Bourgeois, V. Heurgué-Hamard, D. L. J. Lafontaine, M. Graille, The DEAH-box RNA helicase Dhr1 contains a remarkable carboxyl terminal domain essential for small ribosomal subunit biogenesis. *Nucleic Acids Res.* **47**, 7548–7563 (2019). doi:10.1093/nar/gkz529 Medline

32. J. Zhu, X. Liu, M. Anjos, C. C. Correll, A. W. Johnson, Utp14 recruits and activates the RNA helicase Dhr1 to undock U3 snoRNA from the preribosome. *Mol. Cell. Biol.* **36**, 965–978 (2016). doi:10.1128/MCB.00773-15 Medline

33. P. Choudhury, P. Hackert, I. Memet, K. E. Sloan, M. T. Bohnsack, The human RNA helicase DHX37 is required for release of the U3 snoRNP from pre-ribosomal particles. *RNA Biol.* **16**, 54–68 (2019). doi:10.1080/15476286.2018.1556149 Medline

34. G. R. Wells, F. Weichmann, D. Colvin, K. E. Sloan, G. Kudla, D. Tollervey, N. J. Watkins, C. Schneider, The PIN domain endonuclease Utp24 cleaves pre-ribosomal RNA at two coupled sites in yeast and humans. *Nucleic Acids Res.* **44**, 5399–5409 (2016). doi:10.1093/nar/gkw213 Medline

35. K. I. Farley-Barnes, L. M. Ogawa, S. J. Baserga, Ribosomopathies: Old concepts, new controversies. *Trends Genet.* **35**, 754–767 (2019). doi:10.1016/j.tig.2019.07.004 Medline

36. J. C. Ulirsch, J. M. Verboon, S. Kazerounian, M. H. Guo, D. Yuan, L. S. Ludwig, R. E. Handsaker, N. J. Abdulhay, C. Fiorini, G. Genovese, E. T. Lim, A. Cheng, B. B. Cummings, K. R. Chao, A. H. Beggs, C. A. Genetti, C. A. Sieff, P. E. Newburger, E. Niewiadomska, M. Matysiak, A. Vlachos, J. M. Lipton, E. Atsidaftos, B. Glader, A. Narla, P.-E. Gleizes, M.-F. O'Donohue, N. Montel-Lehry, D. J. Amor, S. A. McCarroll, A. H. O'Donnell-Luria, N. Gupta, S. B. Gabriel, D. G. MacArthur, E. S. Lander, M. Lek, L. Da Costa, D. G. Nathan, A. A. Korostelev, R. Do, V. G. Sankaran, H. T. Gazda, The

genetic landscape of Diamond-Blackfan anemia. *Am. J. Hum. Genet.* **103**, 930–947 (2018). doi:10.1016/j.ajhg.2018.10.027 Medline

37. N. Draptchinskaia, P. Gustavsson, B. Andersson, M. Pettersson, T.-N. Willig, I. Dianzani, S. Ball, G. Tchernia, J. Klar, H. Matsson, D. Tentler, N. Mohandas, B. Carlsson, N. Dahl, The gene encoding ribosomal protein S19 is mutated in Diamond-Blackfan anaemia. *Nat. Genet.* **21**, 169–175 (1999). doi:10.1038/5951 Medline

38. J. Flygare, A. Aspesi, J. C. Bailey, K. Miyake, J. M. Caffrey, S. Karlsson, S. R. Ellis, Human *RPS19*, the gene mutated in Diamond-Blackfan anemia, encodes a ribosomal protein required for the maturation of 40S ribosomal subunits. *Blood* **109**, 980–986 (2007). doi:10.1182/blood-2006-07-038232 Medline

39. J. R. P. Knight, A. E. Willis, J. Milner, Active regulator of SIRT1 is required for ribosome biogenesis and function. *Nucleic Acids Res.* **41**, 4185–4197 (2013). doi:10.1093/nar/gkt129 Medline

40. N. Maeda, S. Toku, N. Kenmochi, T. Tanaka, A novel nucleolar protein interacts with ribosomal protein S19. *Biochem. Biophys. Res. Commun.* **339**, 41–46 (2006). doi:10.1016/j.bbrc.2005.10.184 Medline

41. B. L. Ebert, J. Pretz, J. Bosco, C. Y. Chang, P. Tamayo, N. Galili, A. Raza, D. E. Root, E. Attar, S. R. Ellis, T. R. Golub, Identification of *RPS14* as a 5q- syndrome gene by RNA interference screen. *Nature* **451**, 335–339 (2008). doi:10.1038/nature06494 Medline

42. N. A. Paolini, M. Attwood, S. B. Sondalle, C. M. D. S. Vieira, A. M. van Adrichem, F. M. di Summa, M.-F. O'Donohue, P.-E. Gleizes, S. Rachuri, J. W. Briggs, R. Fischer, P. J. Ratcliffe, M. W. Wlodarski, R. H. Houtkooper, M. von Lindern, T. W. Kuijpers, J. D. Dinman, S. J. Baserga, M. E. Cockman, A. W. MacInnes, A ribosomopathy reveals decoding defective ribosomes driving human dysmorphism. *Am. J. Hum. Genet.* **100**, 506–522 (2017). doi:10.1016/j.ajhg.2017.01.034 Medline

43. A. G. Marneros, BMS1 is mutated in aplasia cutis congenita. *PLOS Genet.* **9**, e1003573 (2013). doi:10.1371/journal.pgen.1003573 Medline

44. J. Armistead, S. Khatkar, B. Meyer, B. L. Mark, N. Patel, G. Coghlan, R. E. Lamont, S. Liu, J. Wiechert, P. A. Cattini, P. Koetter, K. Wrogemann, C. R. Greenberg, K.-D. Entian, T. Zelinski, B. Triggs-Raine, Mutation of a gene essential for ribosome biogenesis, *EMG1*, causes Bowen-Conradi syndrome. *Am. J. Hum. Genet.* **84**, 728–739 (2009). doi:10.1016/j.ajhg.2009.04.017 Medline

45. P. Chagnon, J. Michaud, G. Mitchell, J. Mercier, J.-F. Marion, E. Drouin, A. Rasquin-Weber, T. J. Hudson, A. Richter, A missense mutation (R565W) in *Cirhin* (FLJ14728) in North American Indian childhood cirrhosis. *Am. J. Hum. Genet.* **71**, 1443–1449 (2002). doi:10.1086/344580 Medline

46. I. M. Slaymaker, L. Gao, B. Zetsche, D. A. Scott, W. X. Yan, F. Zhang, Rationally engineered Cas9 nucleases with improved specificity. *Science* **351**, 84–88 (2016). doi:10.1126/science.aad5227 Medline

47. J.-P. Concordet, M. Haeussler, CRISPOR: Intuitive guide selection for CRISPR/Cas9 genome editing experiments and screens. *Nucleic Acids Res.* **46**, W242–W245 (2018). doi:10.1093/nar/gky354 Medline

48. D. N. Mastronarde, Automated electron microscope tomography using robust prediction of specimen movements. *J. Struct. Biol.* **152**, 36–51 (2005). doi:10.1016/j.jsb.2005.07.007 Medline

49. J. Zivanov, T. Nakane, B. O. Forsberg, D. Kimanius, W. J. H. Hagen, E. Lindahl, S. H. W. Scheres, New tools for automated high-resolution cryo-EM structure determination in RELION-3. *eLife* **7**, e42166 (2018). doi:10.7554/eLife.42166 Medline

50. S. Q. Zheng, E. Palovcak, J.-P. Armache, K. A. Verba, Y. Cheng, D. A. Agard, MotionCor2: Anisotropic correction of beam-induced motion for improved cryo-electron microscopy. *Nat. Methods* **14**, 331–332 (2017). doi:10.1038/nmeth.4193 Medline

51. K. Zhang, Gctf: Real-time CTF determination and correction. *J. Struct. Biol.* **193**, 1–12 (2016). doi:10.1016/j.jsb.2015.11.003 Medline

52. T. Wagner, F. Merino, M. Stabrin, T. Moriya, C. Antoni, A. Apelbaum, P. Hagel, O. Sitsel, T. Raisch, D. Prumbaum, D. Quentin, D. Roderer, S. Tacke, B. Siebolds, E. Schubert, T. R. Shaikh, P. Lill, C. Gatsogiannis, S. Raunser, SPHIRE-crYOLO is a fast and accurate fully automated particle picker for cryo-EM. *Commun. Biol.* **2**, 218 (2019). doi:10.1038/s42003-019-0437-z Medline

53. J. Zivanov, T. Nakane, S. H. W. Scheres, Estimation of high-order aberrations and anisotropic magnification from cryo-EM data sets in *RELION*-3.1. *IUCrJ* **7**, 253–267 (2020). doi:10.1107/S2052252520000081 Medline

54. T. C. Terwilliger, S. J. Ludtke, R. J. Read, P. D. Adams, P. V. Afonine, Improvement of cryo-EM maps by density modification. *Nat. Methods* **17**, 923–927 (2020). doi:10.1038/s41592-020-0914-9 Medline

55. D. Liebschner, P. V. Afonine, M. L. Baker, G. Bunkóczi, V. B. Chen, T. I. Croll, B. Hintze, L.-W. Hung, S. Jain, A. J. McCoy, N. W. Moriarty, R. D. Oeffner, B. K. Poon, M. G. Prisant, R. J. Read, J. S. Richardson, D. C. Richardson, M. D. Sammito, O. V. Sobolev, D. H. Stockwell, T. C. Terwilliger, A. G. Urzhumtsev, L. L. Videau, C. J. Williams, P. D. Adams, Macromolecular structure determination using X-rays, neutrons and electrons: Recent developments in *Phenix*. *Acta Crystallogr. D* **75**, 861–877 (2019). doi:10.1107/S2059798319011471 Medline

56. P. B. Rosenthal, R. Henderson, Optimal determination of particle orientation, absolute hand, and contrast loss in single-particle electron cryomicroscopy. *J. Mol. Biol.* **333**, 721–745 (2003). doi:10.1016/j.jmb.2003.07.013 Medline

57. S. Chen, G. McMullan, A. R. Faruqi, G. N. Murshudov, J. M. Short, S. H. W. Scheres, R. Henderson, High-resolution noise substitution to measure overfitting and validate resolution in 3D structure determination by single particle electron cryomicroscopy. *Ultramicroscopy* **135**, 24–35 (2013). doi:10.1016/j.ultramic.2013.06.004 Medline

58. J. B. Heymann, Guidelines for using Bsoft for high resolution reconstruction and validation of biomolecular structures from electron micrographs. *Protein Sci.* **27**, 159–171 (2018). doi:10.1002/pro.3293 Medline

59. A. Punjani, J. L. Rubinstein, D. J. Fleet, M. A. Brubaker, cryoSPARC: Algorithms for rapid unsupervised cryo-EM structure determination. *Nat. Methods* **14**, 290–296 (2017). doi:10.1038/nmeth.4169 Medline

60. B. Webb, A. Sali, Protein structure modeling with MODELLER. *Methods Mol. Biol.* **2199**, 239–255 (2021). doi:10.1007/978-1-0716-0892-0_14 Medline

61. J. Pfab, N. M. Phan, D. Si, DeepTracer for fast de novo cryo-EM protein structure modeling and special studies on CoV-related complexes. *Proc. Natl. Acad. Sci. U.S.A.* **118**, e2017525118 (2021). doi:10.1073/pnas.2017525118 Medline

62. A. Casañal, B. Lohkamp, P. Emsley, Current developments in *Coot* for macromolecular model building of Electron Cryo-microscopy and Crystallographic Data. *Protein Sci.* **29**, 1069–1078 (2020). doi:10.1002/pro.3791 Medline

63. J. Yang, I. Anishchenko, H. Park, Z. Peng, S. Ovchinnikov, D. Baker, Improved protein structure prediction using predicted interresidue orientations. *Proc. Natl. Acad. Sci. U.S.A.* **117**, 1496–1503 (2020). doi:10.1073/pnas.1914677117 Medline

64. P. V. Afonine, B. K. Poon, R. J. Read, O. V. Sobolev, T. C. Terwilliger, A. Urzhumtsev, P. D. Adams, Real-space refinement in PHENIX for cryo-EM and crystallography. *Acta Crystallogr. D* **74**, 531–544 (2018). doi:10.1107/S2059798318006551 Medline

65. E. F. Pettersen, T. D. Goddard, C. C. Huang, G. S. Couch, D. M. Greenblatt, E. C. Meng, T. E. Ferrin, UCSF Chimera—A visualization system for exploratory research and analysis. *J. Comput. Chem.* **25**, 1605–1612 (2004). doi:10.1002/jcc.20084 Medline

66. E. F. Pettersen, T. D. Goddard, C. C. Huang, E. C. Meng, G. S. Couch, T. I. Croll, J. H. Morris, T. E. Ferrin, UCSF ChimeraX: Structure visualization for researchers, educators, and developers. *Protein Sci.* **30**, 70–82 (2021). doi:10.1002/pro.3943 Medline

67. The PyMOL Molecular Graphics System, Version 2.0 (Schrödinger, LLC, 2017).

68. P. D. Adams, P. V. Afonine, G. Bunkóczi, V. B. Chen, I. W. Davis, N. Echols, J. J. Headd, L.-W. Hung, G. J. Kapral, R. W. Grosse-Kunstleve, A. J. McCoy, N. W. Moriarty, R. Oeffner, R. J. Read, D. C. Richardson, J. S. Richardson, T. C. Terwilliger, P. H. Zwart, *PHENIX*: A comprehensive Python-based system for macromolecular structure solution. *Acta Crystallogr. D* **66**, 213–221 (2010). doi:10.1107/S0907444909052925 Medline

69. P. Emsley, K. Cowtan, *Coot*: Model-building tools for molecular graphics. *Acta Crystallogr. D* **60**, 2126–2132 (2004). doi:10.1107/S0907444904019158 Medline

70. J.-H. Kim, A. T. Dilthey, R. Nagaraja, H.-S. Lee, S. Koren, D. Dudekula, W. H. Wood Iii, Y. Piao, A. Y. Ogurtsov, K. Utani, V. N. Noskov, S. A. Shabalina, D. Schlessinger, A. M. Phillippy, V. Larionov, Variation in human chromosome 21 ribosomal RNA genes characterized by TAR cloning and long-read sequencing. *Nucleic Acids Res.* **46**, 6712–6725 (2018). doi:10.1093/nar/gky442 Medline

71. F. Sievers, A. Wilm, D. Dineen, T. J. Gibson, K. Karplus, W. Li, R. Lopez, H. McWilliam, M. Remmert, J. Söding, J. D. Thompson, D. G. Higgins, Fast, scalable generation of high-quality protein multiple sequence alignments using Clustal Omega. *Mol. Syst. Biol.* **7**, 539 (2011). doi:10.1038/msb.2011.75 Medline

72. H. Ashkenazy, S. Abadi, E. Martz, O. Chay, I. Mayrose, T. Pupko, N. Ben-Tal, ConSurf 2016: An improved methodology to estimate and visualize evolutionary conservation in macromolecules. *Nucleic Acids Res.* **44**, W344–W350 (2016). doi:10.1093/nar/gkw408 Medline

73. D. W. A. Buchan, D. T. Jones, The PSIPRED Protein Analysis Workbench: 20 years on. *Nucleic Acids Res.* **47**, W402–W407 (2019). doi:10.1093/nar/gkz297 Medline

74. Y. Z. Tan, P. R. Baldwin, J. H. Davis, J. R. Williamson, C. S. Potter, B. Carragher, D. Lyumkis, Addressing preferred specimen orientation in single-particle cryo-EM through tilting. *Nat. Methods* **14**, 793–796 (2017). doi:10.1038/nmeth.4347 Medline

75. R. Lorenz, S. H. Bernhart, C. Höner Zu Siederdissen, H. Tafer, C. Flamm, P. F. Stadler, I. L. Hofacker, ViennaRNA Package 2.0. *Algorithms Mol. Biol.* **6**, 26 (2011). doi:10.1186/1748-7188-6-26 Medline

76. M. Popenda, M. Szachniuk, M. Antczak, K. J. Purzycka, P. Lukasiak, N. Bartol, J. Blazewicz, R. W. Adamiak, Automated 3D structure composition for large RNAs. *Nucleic Acids Res.* **40**, e112 (2012). doi:10.1093/nar/gks339 Medline